TUBB4B is essential for the cytoskeletal architecture of cochlear supporting cells and motile cilia development

Check for updates

Urikhan Sanzhaeva[1], Helen Boyd-Pratt[2], Philip T. R. Bender[3], Thamaraiselvi Saravanan[1], Scott B. Rhodes[1], Tongju Guan[1], Neil Billington [1], Shannon E. Boye[4], Christopher L. Cunningham [5], Charles T. Anderson [3] & Visvanathan Ramamurthy [1,6] ✉

Microtubules are essential for various cellular processes. The functional diversity of microtubules is attributed to the incorporation of various α- and β-tubulin isotypes encoded by different genes. In this work, we investigated the functional role of β4B-tubulin isotype (TUBB4B) in hearing and vision as mutations in *TUBB4B* are associated with sensorineural disease. Using a *Tubb4b* knockout mouse model, our findings demonstrate that TUBB4B is essential for hearing. Mice lacking TUBB4B are profoundly deaf due to defects in the inner and middle ear. Specifically, in the inner ear, the absence of TUBB4B lead to disorganized and reduced densities of microtubules in pillar cells, suggesting a critical role for TUBB4B in providing mechanical support for auditory transmission. In the middle ear, *Tubb4b*^{−/−} mice exhibit motile cilia defects in epithelial cells, leading to the development of otitis media. However, *Tubb4b* deletion does not affect photoreceptor function or cause retinal degeneration. Intriguingly, β6-tubulin levels increase in retinas lacking β4B-tubulin isotype, suggesting a functional compensation mechanism. Our findings illustrate the essential roles of TUBB4B in hearing but not in vision in mice, highlighting the distinct functions of tubulin isotypes in different sensory systems.

Microtubules are ubiquitous cytoskeletal filaments essential in the function of eukaryotic cells. These polymers, composed of polymerized αβ-tubulin heterodimers, are critical in cell division as they form mitotic/meiotic spindles that separate chromosomes[1]. Microtubules are also involved in intracellular transport. They form tracks along which motor proteins carrying vesicles and organelles move[1,2]. In addition, microtubules form the axoneme of cilia and flagella, organelles responsible for sensing the extracellular environment and facilitating motility. Central to the functional diversity and properties of microtubules is the incorporation of different tubulin isotypes, each encoded by distinct genes. The post-translational modification of tubulin also influences the microtubule mechanical properties, dynamics, and the binding of microtubule-associated proteins[3,4].

Despite the fundamental roles of microtubules in cells, mutations in tubulin genes can result in various tissue-specific effects such as brain malformations, infertility, primary ciliary dyskinesia (PCD), hearing, and vision loss[5–9]. Typically, disease-associated mutations of human tubulin genes are heterozygous missense mutations rather than gene deletions, nonsense, or frameshift mutations. This pattern of disease inheritance suggests a dominant-interfering mechanism, wherein these mutant tubulin subunits, when incorporated into microtubules, can disrupt microtubule function. The presence of such mutations can adversely affect microtubule dynamics, the interaction with microtubule-associated proteins, and the stability of heterodimers[10,11]. The association between distinct tubulin isotypes and specific human diseases, as well as studies in various species, underscores specialized roles for different tubulin isotypes[12,13].

There are two β4-tubulin isotypes encoded in the mammalian genome, β4A- and β4B-tubulins (TUBB4A, TUBB4B) that share 98% protein sequence identity. Mutations in *TUBB4A* are associated with various neurodegenerative disorders, such as H-ABC leukodystrophy (hypomyelination with atrophy of the basal ganglia and cerebellum)[14] and Whispering dysphonia (DYT4 dystonia)[15], consistent with the prominent expression of this isotype in the brain[16]. Interestingly, *Tubb4a*^{−/−} mice did not exhibit any

[1]Department of Biochemistry and Molecular Medicine, West Virginia University School of Medicine, Morgantown, WV, USA. [2]Clinical Translational Sciences Institute, West Virginia University School of Medicine, Morgantown, WV, USA. [3]Rockefeller Neuroscience Institute and Department of Neuroscience, West Virginia University School of Medicine, Morgantown, WV, USA. [4]Division of Cellular and Molecular Therapy, Department of Pediatrics, University of Florida College of Medicine, Gainesville, FL, USA. [5]Pittsburgh Hearing Research Center, Department of Otolaryngology, University of Pittsburgh, Pittsburgh, PA, USA. [6]Department of Ophthalmology and Visual Sciences, West Virginia University School of Medicine, Morgantown, WV, USA. ✉e-mail: ramamurthyv@hsc.wvu.edu

neurodevelopmental or neurodegenerative defects, and the loss of TUBB4A was compensated by other tubulin isotypes[17].

Recent studies showed that heterozygous missense mutations in the β4B-tubulin isotype (*TUBB4B*) are associated with various diseases, including Leber Congenital Amaurosis (LCA), a childhood blinding disease, sensorineural hearing loss, and primary ciliary dyskinesia (PCD), a disease caused by defects in motile cilia[6,9,18–20]. Studies using a monoclonal antibody against β4-tubulin isotypes demonstrated β4-tubulin localization to motile and non-motile cilia, including photoreceptor cilia[21–23]. Altogether, the association of *TUBB4B* mutations with severe vision loss and PCD, and ciliary localization of β4-tubulin suggests a role for β4B-tubulin in ciliated tissues, including the retina. Indeed, studies using *Tubb4b* knockout mice have demonstrated that β4B-tubulin is essential for motile ciliogenesis, and the absence of this particular β-tubulin isotype leads to defects in motile cilia number and length[9,24]. However, the functional role of TUBB4B in hearing and the mechanisms behind hearing loss caused by *TUBB4B* mutations remains unclear.

The organ of Corti, located within the cochlea in the inner ear, is responsible for converting sound stimuli into electrical signals processed in the brain. The organ of Corti is comprised of sensory hair cells and supporting cells. One row of inner hair cells is separated from three rows of outer hair cells by supporting cells, inner and outer pillar cells. The outer hair cells are located on top of Deiters' cells, another subtype of supporting cells. On the apical surface, sensory hair cells contain hair bundles, actin-based structures responsible for converting mechanical input into electrical signals. The hair bundles of cochlear hair cells are arranged in a staircase pattern and uniformly oriented along the medial-lateral axis of the organ of Corti. Despite the name, stereocilia are not true cilia and do not contain microtubules. However, the kinocilium, a specialized primary cilium present in hair cells, is critical for establishing the shape and orientation of stereociliary bundles during development. However, the kinocilium eventually degenerates before the onset of hearing in mammals[25]. Although there are some microtubules present in the cell body of hair cells and kinocilium, microtubules are dominant cytoskeletal filaments in two supporting cell types, Deiters' and pillar cells. Each cell type contains hundreds to thousands of tightly organized microtubules cross-linked to actin[26]. The microtubules of the pillar and Deiters' cells provide them with mechanical properties that assist in transmitting sound energy through the cochlea[26–28]. Interestingly, studies using a monoclonal antibody against β4-tubulin demonstrated β4-tubulin expression in pillar and Deiters' cells in the rat organ of Corti[29]. Thus, the link between *TUBB4B* mutations and sensorineural hearing loss suggests that this β-tubulin isotype may be essential either for structure and/or function of kinocilia or microtubules of pillar and Deiters' cells.

In this study, we focused on the role of β4B-tubulin in hearing and vision. Using a *Tubb4b* knockout (*Tubb4b*⁻/⁻) murine model, we found that mice lacking β4B-tubulin were profoundly deaf. Intriguingly, in the inner ear, the absence of β4B-tubulin did not lead to cochlear hair cell degeneration, defects in kinocilia structure, or alterations in stereocilia organization. Notably, lack of β4B-tubulin resulted in decreased microtubule density and disorganization of microtubule bundles in pillar cells with no major changes in Deiters' cells. In addition, we discovered that in the middle ear, *Tubb4b*⁻/⁻ mice develop otitis media caused by defective motile cilia of epithelial cells lining the middle ear cavity. Surprisingly, we found that β4B-tubulin is not essential in the murine retina, as photoreceptor function and retinal morphology were unaffected. As a possible compensatory mechanism, we discovered that β6-tubulin transcript and protein levels were upregulated in the retina lacking β4B-tubulin. These findings indicate that *Tubb4b*⁻/⁻ mice faithfully phenocopies hearing phenotypes but fails to recapitulate the vision loss that is seen in patients with *TUBB4B* mutations.

Results

Generation and characterization of *Tubb4b*⁻/⁻ animal model

To investigate the role of β4B-tubulin (TUBB4B) in vision and hearing, we utilized *Tubb4b* knockout (KO; *Tubb4b*⁻/⁻) mice obtained from The Jackson Laboratory. This line, generated by the Knockout Mouse Phenotyping

Program (KOMP), was modified using gRNAs that targeted introns 1 and 3. CRISPR-Cas9 mediated excision resulted in the deletion of exons 2 and 3, leading to premature termination of the protein (Fig. 1A). To validate the *Tubb4b*⁻/⁻ model, we analyzed the protein and mRNA levels of Tubb4b in these mice (Fig. 1B, C). Immunoblotting of protein extracts from the retina of control and *Tubb4b*⁻/⁻ mice revealed an 84% reduction of β4-tubulin (TUBB4) in the retina of knockout mice (Fig. 1B, left panel). It is important to note that the β4-tubulin antibody we used does not distinguish between β4B- (TUBB4B) and β4A-tubulins (TUBB4A)[30,31]. To further investigate the decrease in TUBB4B, we performed reverse transcription PCR (RT-PCR) of mRNA extracted from wildtype and mutant retinas. RT-PCR using primers targeting the 5' untranslated region (5' UTR) and exon 4 of *Tubb4b* (Fig. 1A, arrows) produced a 434 base pair (bp) product in wildtype and a truncated *Tubb4b* product (214 bp) in the *Tubb4b*⁻/⁻ mice, consistent with the deletion of exons 2 and 3 (Fig. 1B, right panel). In contrast, RT-PCR using primers targeting the 5'-UTR and exon 4 of the *Tubb4a* resulted in 619 bp product in both *Tubb4b*⁻/⁻ and *Tubb4b*⁺/⁺ mice. Altogether, findings from RT-PCR confirms a specific deficiency of TUBB4B in the mutant retina. In contrast to the retina, immunoblot analysis of cochlear extracts showed an absence of TUBB4 in the *Tubb4b*⁻/⁻ cochleae (Fig. 1C), indicating that TUBB4B is the predominant β4-tubulin isotype expressed in this tissue. Altogether, these results confirm the absence of TUBB4B expression in the *Tubb4b*⁻/⁻ mouse model.

We also analyzed the inheritance pattern of the knockout allele. The number of *Tubb4b*⁻/⁻ knockout pups produced from heterozygous crosses adhered to Mendelian ratios (χ^2 (df = 2, $n = 271$) = 1.68; P value = 0.57) (Fig. 1D). However, *Tubb4b*⁻/⁻ mice were significantly smaller in size than their wildtype (WT) littermates (P value = 1.3×10^{-4} for 1-month-old male mice; P value = 2.8×10^{-4} for 1-month-old female mice) (Fig. 1E, F). These mice also displayed varying degrees of hydrocephaly (data not shown) and increased lethality with age. Nevertheless, several knockout animals without apparent hydrocephalus survived up to 1 year, suggesting a spectrum of phenotypic severity in the absence of TUBB4B.

β4B-tubulin is expressed in supporting and sensory hair cells of the organ of Corti

Mutations in *TUBB4B* are associated with sensorineural hearing loss (SNHL)[6,9,18–20]. Therefore, we assessed β4B-tubulin expression in the inner ear of neonatal and adult mice. Using immunofluorescence staining, we examined cochlear cryosections for β4-tubulin expression using a TUBB4 antibody. The sections were also stained with markers for sensory hair cells (MYO7A) or supporting cells (GAS2)[28], revealing the presence of β4-tubulin in cochlear sensory hair cells and supporting cells, including pillar and Deiters' cells (Fig. 2). As the TUBB4 antibody cannot distinguish between TUBB4A and TUBB4B, we also immunostained cochlear cryosections from *Tubb4b*⁻/⁻ mice. In cochlear cryosections from these mice, there was no apparent TUBB4 signal (Fig. 2A–A'), providing additional evidence that TUBB4B is the predominant β4-tubulin isotype in cochlear cells. This finding was further supported by the absence of TUBB4 in cochlear lysates of *Tubb4b*⁻/⁻ mice, as demonstrated by immunoblotting (Fig. 1C).

In the postnatal day 4 (P4) neonates, we observed expression of TUBB4B in pillar and cochlear sensory cells (Fig. 2A). In 1-month-old mice, immunofluorescence staining of cochlear cryosections showed robust expression of TUBB4B in the inner pillar, outer pillar, and Deiters' cells (Fig. 2A'–B). TUBB4B-positive microtubules in the pillar and Deiters' cells span the entire cochlear sensory epithelium, from the basilar membrane to the reticular lamina (Fig. 2A'–B). In 1-month-old mice, TUBB4B was also found in outer and inner hair cells (Fig. 2C–C'). It is worth noting that TUBB4B staining was more pronounced in inner hair cells compared to outer hair cells, which is consistent with the known difference in microtubule abundance between the inner and outer hair cells[32] (Fig. 2C–C'). Further, immunostaining of cochlear whole mounts revealed the localization of TUBB4B to microtubules in the apical surface of pillar cells and the phalangeal processes of Deiters' cells (Fig. 2D, E). These findings, taken together, suggest that sensorineural hearing loss (SNHL) caused by
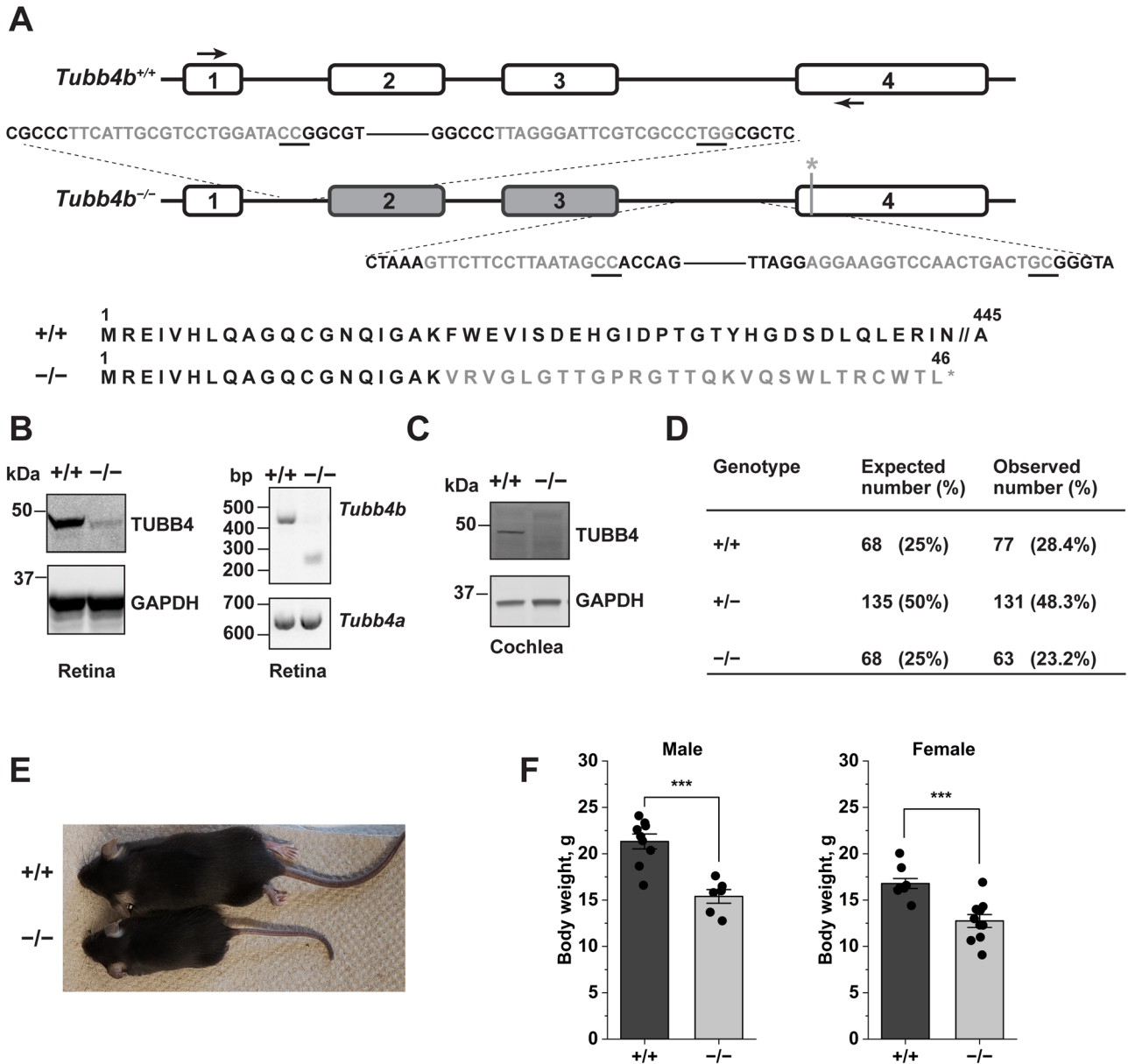
Fig. 1 | Validation of the *Tubb4b*⁻/⁻ murine model. A Schematic illustrating the mutation in *Tubb4b* generated by CRISPR-Cas9. gRNA sequences targeting the introns are shown in grey, with the protospacer adjacent motif (PAM) sequence underlined. Deletion of exons 2 and 3 led to changes to the amino acid sequence (grey) and introduces a premature stop codon (grey asterisk). Arrows in exons 1 and 4 indicate the locations of forward and reverse primers used for RT-PCR. **B** Left panel: Immunoblot of retinal lysates from P30 animals probed with TUBB4 antibody. The blots were also probed for GAPDH, a housekeeping protein serving as a control for protein loading. Molecular weights in kDa are indicated on the left. Right panel: RT-PCR analysis of the *Tubb4b* and *Tubb4a* mRNA extracted from retinal tissue, followed by agarose gel electrophoresis. Markers in base pairs (bp) are indicated on the left. Expected sizes for *Tubb4b* and *Tubb4a* are 434 bp and 619 bp, respectively. **C** Immunoblot of cochlear lysates from 1-month-old *Tubb4b*⁻/⁻ and wildtype littermates, probed with TUBB4 and GAPDH antibodies. All experiments were replicated at least three times with littermates as controls (+/+). **D** The number of pups obtained from *Tubb4b*⁺/⁻ crosses followed Mendelian ratios (total number of animals counted 271). Expected numbers were calculated as (total number of animals counted) * expected ratio (0.25 for +/+, − /−; 0.5 for +/−). The percentage of pups born for each genotype are indicated in the brackets. **E** Image of 1-month-old male *Tubb4b*⁻/⁻ and control littermate. **F** Whole bodyweight of *Tubb4b*⁻/⁻ and control littermates at 1 month. Data are presented as mean ± SEM. ***P value ≤ 0.001.

mutations in *TUBB4B* may arise from abnormalities in sensory hair cells, as well as in the pillar and Deiters' cells.

Loss of TUBB4B leads to profound deafness without hair cell degeneration

We next assessed whether TUBB4B is required for hearing in mice by recording click-evoked Auditory Brainstem Responses (ABRs) in *Tubb4b*⁻/⁻ mice. We recorded ABRs and then determined hearing thresholds, defined as the lowest sound pressure level that generates a detectable response, in 1-month-old *Tubb4b*⁻/⁻ and their control littermates. Mice lacking TUBB4B showed profound deafness, with no response to click stimuli even at 90 dB SPL, the highest level tested. In contrast, in the wildtype controls, the average click ABR threshold was 60 dB SPL (Fig. 3A, B).

Given the importance of kinocilium, which is a microtubule based-structure, in the stereociliary bundle development and orientation[25], we examined the health of primary cilia in the P4 organ of Corti. Immunofluorescence staining of cochlear whole mounts with a ciliary marker (ARL13B) revealed TUBB4B localization to the primary cilia in both hair and supporting cells of the organ of Corti (Fig. S1A). The overall length of OHC kinocilia was unaffected in the absence of TUBB4B (Fig. S1B).
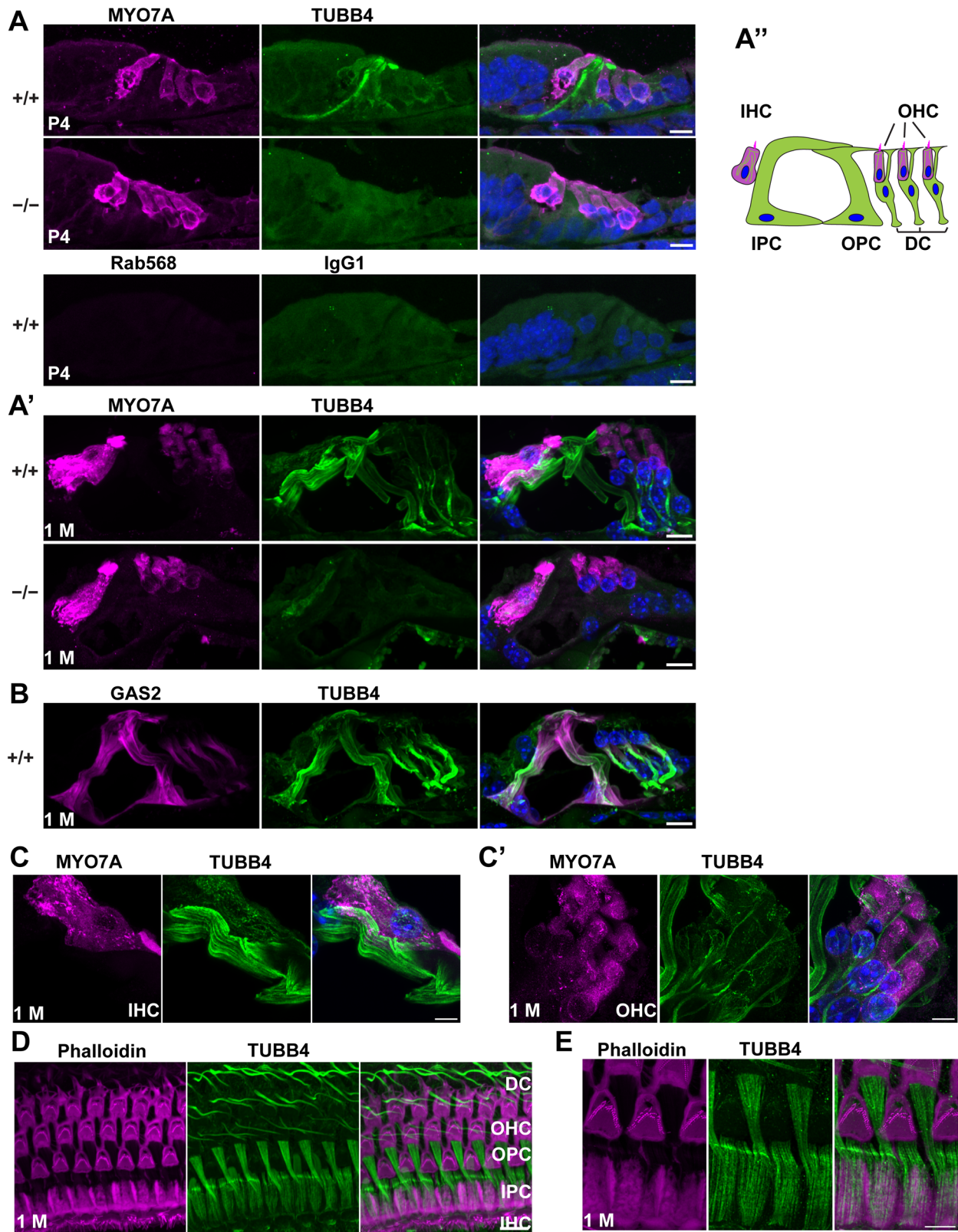
Interestingly, the IHC kinocilia length was slightly reduced in *Tubb4b*$^{-/-}$ mice (Fig. S1C). Additionally, there was no difference in the length of the organ of Corti in the absence of TUBB4B (Fig. S1D). Altogether, these results indicate no major developmental defects but minor deficits in IHC kinocilia length.

We further evaluated the function of outer hair cells (OHCs) using the distortion-product otoacoustic emissions (DPOAEs)[33]. DPOAEs are generated by OHCs when two pure tones separated by a fixed ratio are presented simultaneously into the ear. *Tubb4b*$^{-/-}$ mice had reduced DPOAE amplitudes (Fig. 3C, D), suggesting defects in OHC function.

Fig. 2 | TUBB4B is expressed in cochlear hair cells and supporting cells.
A Cochlear cross-sections at P4 from wildtype controls and *Tubb4b$^{-/-}$* littermates, stained with TUBB4 (green), MYO7A (magenta) antibodies, and DAPI (blue). The bottom panel shows the IgG1 isotype control. Scale bar = 10 μm. **A'** Cochlear cross-sections from 1-month-old *Tubb4b$^{+/+}$* and *Tubb4b$^{-/-}$* mice stained with TUBB4 (green), MYO7A (magenta) antibodies, and DAPI (blue). Scale bar = 10 μm. **A"** Schematic illustration of TUBB4B expression in 1-month-old cochlear cross-sections, showing TUBB4B (green) and MYO7A (magenta). **B** Cochlear cross-sections from 1-month-old *Tubb4b$^{+/+}$* mice stained with TUBB4 (green), GAS2 (magenta) antibodies, and DAPI (blue). Scale bar = 10 μm. **C** High-resolution confocal images

of inner hair cell (IHC) in cochlear cross-section stained with TUBB4 (green), MYO7A (magenta) antibodies, and DAPI (blue). Scale bar = 5 μm. **C'** High-resolution confocal images of outer hair cells (OHC) in cochlear cross-section stained with TUBB4 (green), MYO7A (magenta, hair cells marker) antibodies, and DAPI (blue). Scale bar = 5 μm. **D** Cochlear wholemount from 1-month-old mice stained with TUBB4 (green) antibody and phalloidin (magenta). Scale bar = 10 μm. **E** High-resolution confocal images of pillar cells (PC) and phalangeal process of Deiters' cell (DC) from cochlear whole mounts, stained with TUBB4 (green) antibody and phalloidin (magenta). Scale bar = 5 μm. IHC inner hair cell, IPC inner pillar cell, OPC outer pillar cell, OHC outer hair cell, DC Deiters' cell.
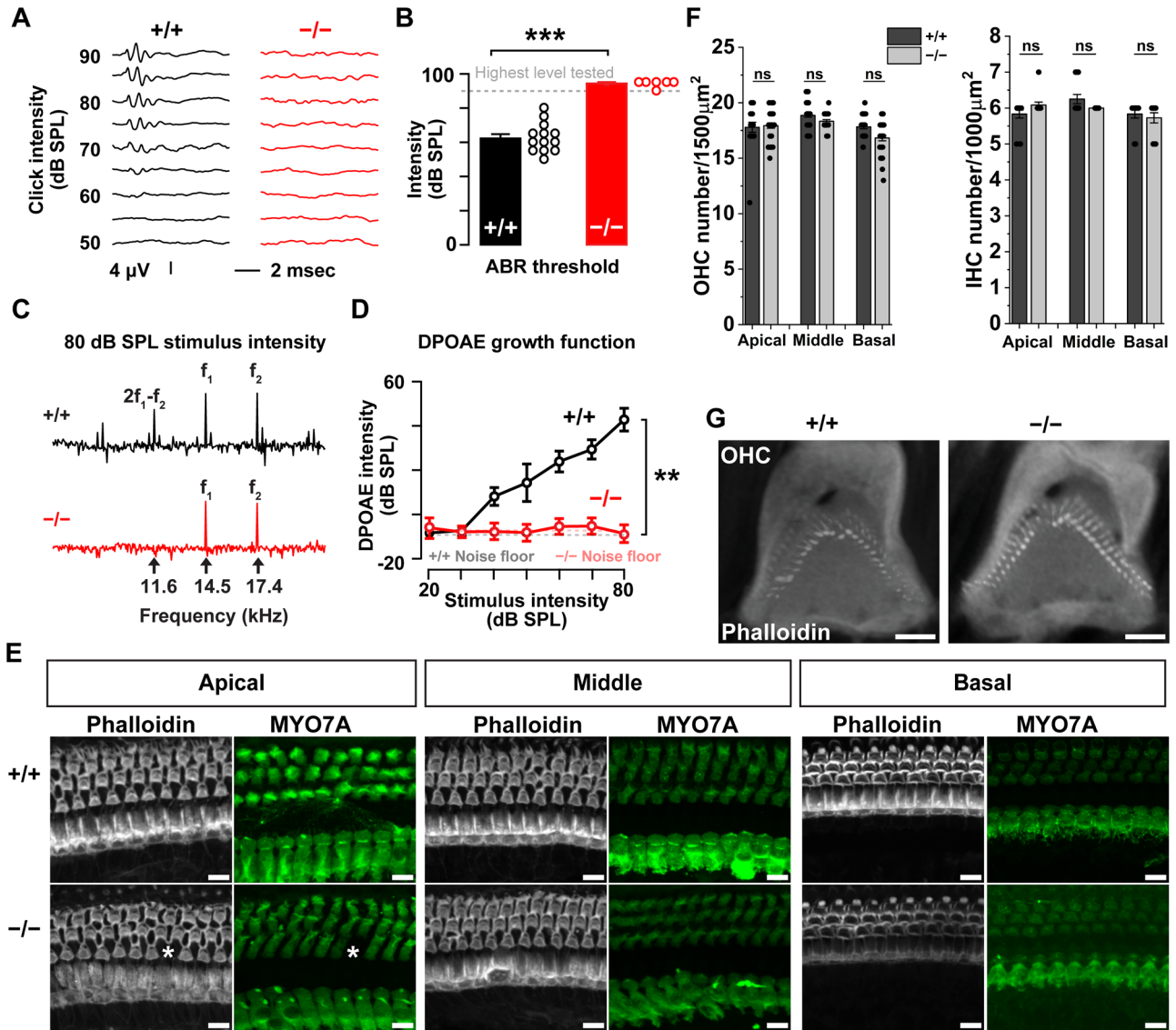
Fig. 3 | *Tubb4b$^{-/-}$* are profoundly deaf without significant hair cell degeneration.
A Representative auditory brainstem response (ABR) traces elicited by clicks in 1-month-old *Tubb4b$^{-/-}$* mice (red) and control littermates (black). Click ABR thresholds measured from 1-month-old *Tubb4b$^{-/-}$* mice (*n* = 6, red) and control littermates (*n* = 13, black). Statistical analysis was conducted using an unpaired two-tailed *t* test. ***Denotes a significance level of *P* < 0.001. **C** Representative distortion product otoacoustic emissions (DPOAE) traces at 16 kHz from 1-month-old *Tubb4b$^{-/-}$* mice (red) and control littermates (black). **D** DPOAE input/output function at 16 kHz frequency from 1-month-old *Tubb4b$^{-/-}$* mice (*n* = 7, red) and control littermates (*n* = 5, black) recorded at each stimulus intensity level. Dashed lines denote the noise floor during the recordings. Statistical analysis was

conducted using a two-way ANOVA. **Denotes a significance level of *P* < 0.01 between genotypes. **E** Cochlear whole mounts from apical, middle, and basal turns of 1-month-old wildtype and *Tubb4b$^{-/-}$* littermates, stained with phalloidin (gray) and MYO7A (green) antibody. Missing outer hair cells are denoted with an asterisk. Scale bar = 10 μm. **F** Quantification of outer hair cells (OHC) and inner hair cells (IHC) in *Tubb4b$^{-/-}$* and control littermates at 1 month. Regions of interest (50 μm × 30 μm for OHC or 50 μm × 20 μm for IHC) were selected in each cochlear turn, and the numbers of hair cells were manually counted. ns not significant. **G** High-resolution confocal images of OHCs from *Tubb4b$^{-/-}$* and control cochlear whole mounts at 1 month, stained with phalloidin (gray). Scale bar = 1 μm. Data are presented as mean ± SEM.

Next, we examined whether the absence of TUBB4B leads to hair cell degeneration. Surprisingly, cochlear whole mounts stained with phalloidin and MYO7A, a hair cell marker, revealed no significant hair cell loss in 1-month-old *Tubb4b*^{−/−} animals across all cochlear turns (Fig. 3E, F). Moreover, the morphology of the stereocilia bundle was indistinguishable between mice lacking TUBB4B and control littermates at 1 month (Figs. 3G and S2).

Microtubules are likely involved in the transport of synaptic ribbon precursors to the presynaptic active zone in cochlear hair cells[34]. Therefore, we examined whether synapse development in hair cells would be affected in mice lacking β4B-tubulin. Immunofluorescence staining of ribbon synapses in cochlear whole mounts with CTBP2 and GluR 2/3, pre- and post-synaptic markers, respectively, revealed no changes in the number of ribbon synapses in mice lacking β4B-tubulin at P20 (Fig. S3A, B), indicating normal synapse development. We also evaluated the presence of functional mechanotransduction channels in IHCs and OHCs by transient incubation with the styryl dye FM1-43FX, which enters the hair cell through the mechanotransduction channels[35]. The uptake of FM1-43FX dye by *Tubb4b*^{−/−} sensory cells suggested that the functional mechanotransduction channels were present (Fig. S3C). Furthermore, we did not observe any defects in the density of spiral ganglion neurons in mice lacking β4B-tubulin (Fig. S3D–F). These findings collectively demonstrate that while TUBB4B is essential for hearing, its absence does not affect hair cell development, maintenance, or the structure of cochlear sensory cells.

TUBB4B is critical for maintaining the cytoskeletal architecture of pillar cells

Microtubules in supporting cells provide pillar and Deiters' cells with the mechanical properties needed to facilitate sound transmission by hair cells throughout the cochlea[26–28]. As the absence of TUBB4B did not result in noticeable defects in sensory hair cells or spiral ganglion neurons, we sought to determine whether the pillar and Deiters' cells were affected in the *Tubb4b*^{−/−} mice.

To assess the overall tubulin levels in the cochlea, we performed immunoblot analysis of cochlear lysates from 1-month-old wildtype controls and *Tubb4b*^{−/−} littermates. The total β-tubulin levels in cochlear lysates were reduced to less than half of that seen in wildtype littermates (Fig. 4A, B, *P* value = 0.058). Further immunofluorescence staining with α-tubulin and acetylated tubulin antibodies on cochlear whole mounts at 1 month revealed decreased microtubule staining on the apical surface of pillar cells and phalangeal processes of Deiters' cells in the *Tubb4b*^{−/−} mice (Fig. 4C), implying a specific decrease in microtubule numbers in these cells. Interestingly, the head length of inner pillar cells (Fig. 4C, double arrow), representing the inner-to-outer hair cell distance, was significantly decreased in mice lacking TUBB4B (Fig. 4D). We observed a reduction in microtubule staining and narrower phalangeal processes and microtubule stalk in the basal region of Deiters' cell in *Tubb4b*^{−/−} mice (Fig. 4E, F). In contrast, the Deiters' cell cup diameter size was unaffected in the absence of TUBB4B (Fig. 4F). Furthermore, Scanning Electron Microscopy (SEM) of the organ of Corti confirmed narrower phalangeal processes in cochlear basal turns in *Tubb4b*^{−/−} mice (Fig. S4A). Interestingly, the phalangeal process diameters measured in cochlear whole mounts immunostained with α-tubulin were unaffected in the apical and middle turns of the organ of Corti in mice lacking TUBB4B (Fig. S4B).

To gain additional insights, we sought to assess the density of microtubules in pillar and Deiters' cells using transmission electron microscopy (TEM) (Fig. 5A–A'). TEM images from transverse sections of the organ of Corti revealed a substantial decrease in microtubule number and density in the inner and outer pillar cells of *Tubb4b*^{−/−} mice (Fig. 5B, C, E, E', F, F'). Moreover, microtubules of outer pillar cells of mutant mice were disorganized when compared to the regularly spaced square array in control littermates (Fig. 5C, bottom panel). In contrast, microtubule number and density in Deiters' cells phalangeal processes were unaffected in the mice lacking TUBB4B (Fig. 5D, G, G'). Altogether, these findings

collectively indicate that TUBB4B plays a critical role in the cytoskeletal organization of pillar cells.

TUBB4B deficiency causes ciliary defects and the development of otitis media

As previous studies have shown that disorganized microtubules in supporting cells of the organ of Corti can lead to hearing loss but not profound deafness in mice[28], we sought to explore potential additional mechanisms contributing to the profound deafness in mice lacking TUBB4B. We examined the middle ear of *Tubb4b*^{−/−} mice since some patients with *TUBB4B* mutations develop otitis media and conductive hearing loss (CHL)[6,9,18]. Indeed, otoscopic and histological analysis revealed the presence of otitis media with effusion in 1-month-old *Tubb4b*^{−/−} animals (Fig. 6A, B), characterized by a cloudy tympanic membrane compared to a translucent membrane in control littermates (Fig. 6A), and effusions filling the middle ear cavities (Fig. 6B, middle panel). We then examined the onset of otitis media by comparing the cross-sections of auditory bullae stained with hematoxylin and eosin (H&E) at various developmental stages. While, the cross-sections of *Tubb4b*^{−/−} and control mice were similar at P10, by P15, effusions filled the middle ear cavities of mutant mice (Fig. 6C).

Mutations in *TUBB4B* are associated with primary cilia dyskinesia (PCD)[9]. This observation is consistent with studies showing ciliary localization of TUBB4[23]. Therefore, we assessed whether TUBB4B is present in the motile cilia in the middle ear. Immunofluorescence staining of P10 auditory bullae cross-sections with β4-tubulin and acetylated tubulin antibodies confirmed the localization of TUBB4B in motile cilia of the epithelial lining of the middle ear cavity. We also noted a weaker staining in cytoplasmic microtubules in control littermates. In contrast, TUBB4 staining was absent in *Tubb4b*^{−/−} middle ear (Fig. 6D). We also examined the health of motile cilia in the middle ear, near the Eustachian tube (Fig. 6B, top panel), and in the dorsal region (Fig. 6B, bottom panel). Our observations in 1-month-old *Tubb4b*^{−/−} mice showed defects in cilia number and length (Fig. 6B). Similar to adult middle ear cross-sections stained with H&E, we observed shortened and fewer cilia in P10 sections, before the onset of otitis media (Fig. 6D, D'). Consistent with this observation, scanning electron microscopy (SEM) of the middle ear from P10 wildtype controls showed well-organized motile cilia of epithelial cells (Fig. 6E). In contrast, in *Tubb4b*^{−/−} mice, cilia density and length were reduced (Fig. 6E, F). Altogether, these findings demonstrate that TUBB4B plays an essential role in maintaining motile cilia in the middle ear, and its absence leads to defective cilia and otitis media with effusions.

## TUBB4B is not essential for photoreceptor development or function in murine retina

As mutations in *TUBB4B* in humans are associated with LCA, a severe blinding disease[6,9,18–20], we hypothesized that TUBB4B plays an essential role in photoreceptor development and function. To evaluate this conjecture, we assessed photoreceptor function using electroretinography (ERG), which measures retina-derived responses to light stimuli[36,37]. The downward trending a-wave is derived from the photoreceptors, while the upward trending b-wave represents responses from downstream neurons, mainly bipolar cells, in the retina. Our results showed that, similar to littermate controls, *Tubb4b*^{−/−} mice exhibited robust rod (scotopic) and cone (photopic) responses to light (Fig. 7A, B). Furthermore, sensitivity curves (Fig. 7C, D) plotted using a-wave (scotopic) and b-wave (photopic) responses of mice aged from P50 to P150 revealed no changes in photoreceptor responses in mutant mice. This finding contrasts the typical LCA presentation in humans, where ERG responses are significantly reduced or absent[38,39]. Additionally, histological analysis using H&E staining of retinal cross-sections from 6-month-old *Tubb4b*^{−/−} mice revealed normal morphology, with the number of photoreceptor nuclei in the outer nuclear layer (ONL), similar to that of control mice (Fig. 7E). Altogether, these findings indicate that TUBB4B is not essential for photoreceptor development and function in mice.
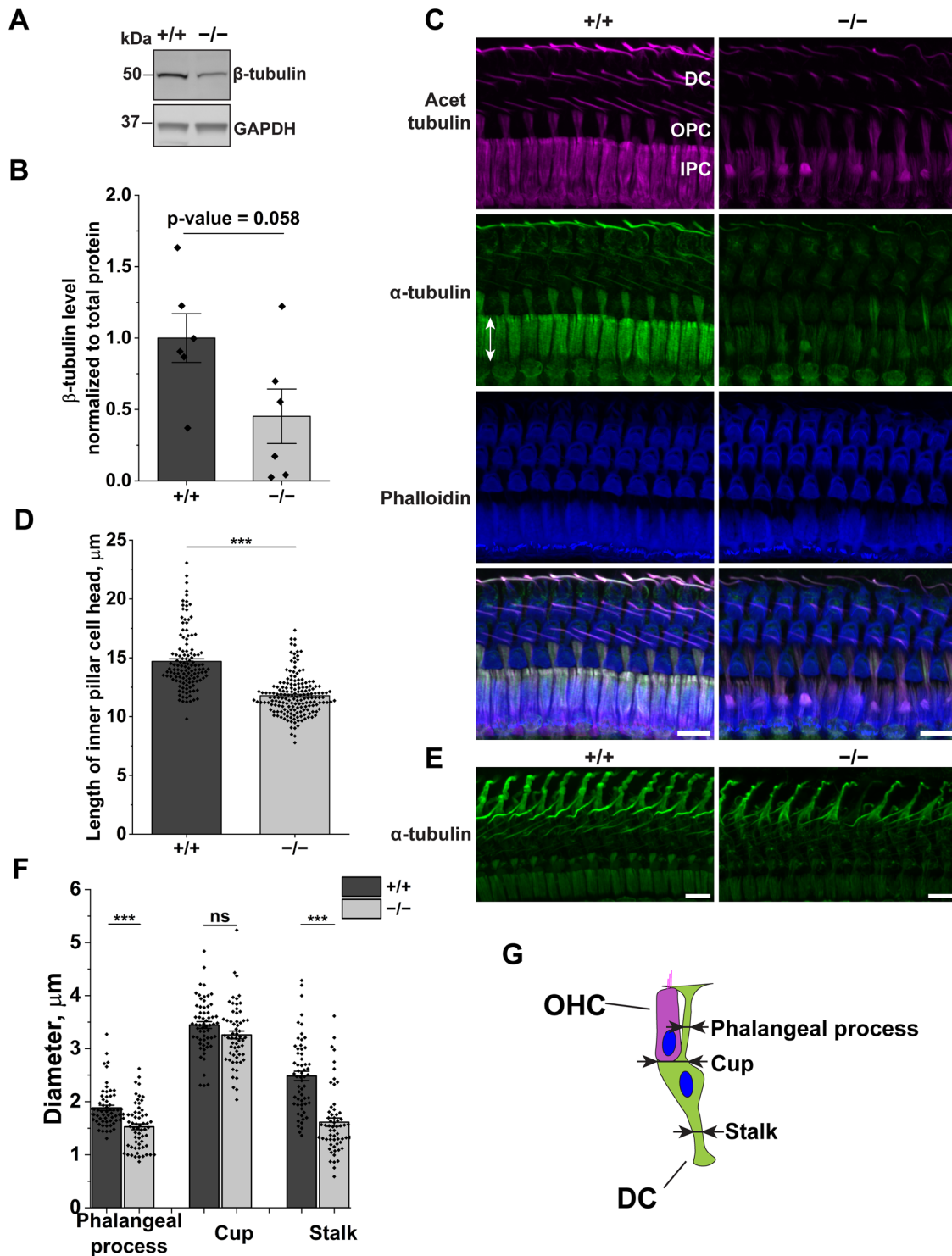
Fig. 4 | The absence of TUBB4B leads to reduction in microtubules.
A Immunoblot analysis of cochlear lysates from 1-month-old wildtype and *Tubb4b*$^{-/-}$ littermates, probed with β-tubulin antibody. The blots were also probed for GAPDH, a housekeeping protein, serving as a loading control. The molecular weights in kDa are indicated on the left. **B** Quantification of β-tubulin levels from (**A**), normalized to total protein. Data are presented as mean ± SEM (*n* = 6, unpaired *t* test, two-tailed). **C** Cochlear whole mounts from 1-month-old mice wildtype and *Tubb4b*$^{-/-}$ littermates, stained with acetylated tubulin (magenta), α-tubulin (green) antibodies, and phalloidin (blue). The double arrow denotes the inner pillar cell head. Scale bar = 10 μm. **D** Inner pillar cell head length measured using acetylated tubulin staining of cochlear whole mounts from the apical turns of 1-month-old

wildtype and *Tubb4b*$^{-/-}$ littermates. Data are presented as mean ± SEM (*n* = 3, Mann–Whitney *U* test). *** denotes a significance level of *P* < 0.001. **E** Cochlear wholemount images from basal turns of 1-month-old wildtype and *Tubb4b*$^{-/-}$ littermates, stained with α-tubulin (green). Scale bar = 10 μm. **F** Deiters' cells phalangeal processes, cup, and stalk diameters measured from basal turns of 1-month-old wildtype and *Tubb4b*$^{-/-}$ littermates, stained with α-tubulin. Data are presented as mean ± SEM (*n* = 3, unpaired *t* test, two-tailed). *** denotes a significance level of *P* < 0.001; ns not significant. **G** Schematic illustration of Deiters' cells phalangeal processes, cup and stalk locations used for diameter measurement. OHC outer hair cell, DC Deiters' cell.
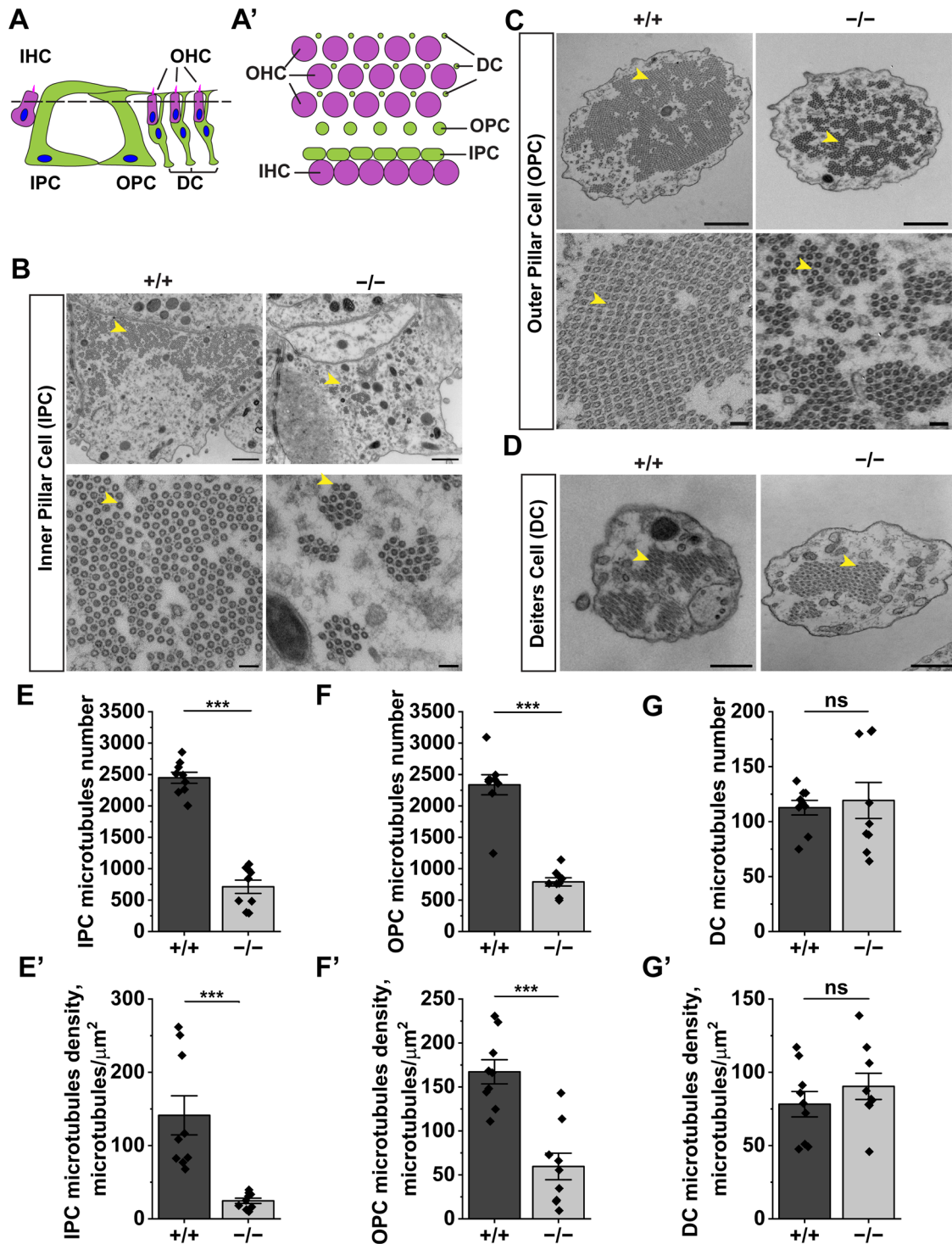
Fig. 5 | The cytoskeletal ultrastructure of supporting cells in the cochlea is dependent on TUBB4B. A Schematic illustration of the organ of Corti in 1-month-old mice, with a dashed line indicating the transverse section plane used for transmission electron microscopy (TEM). **A'** Additional illustration of the organ of Corti, sectioned through the plane shown in (**A**). **B** TEM micrographs of inner pillar cells (IPC). Yellow arrowheads point to microtubule cross-sections. Scale bars: 1 μm (top panel), 100 nm (bottom panel). **C** TEM micrographs of outer pillar cells (OPC), with yellow arrowheads pointing to microtubule cross-sections. Scale bars: 1 μm (top panel), 100 nm (bottom panel). **D** TEM micrographs of Deiters' cells (DC) phalangeal processes, with yellow arrowheads pointing to microtubule cross-sections. Scale bar = 500 nm. **E** Quantification of microtubules number per IPC. **E'**

Quantification of IPC microtubules density (IPC microtubules number per cell cross-section area). **F** Quantification of microtubules number per OPC. **F'** Quantification of OPC microtubules density (OPC microtubules number per cell cross-section area). **G** Quantification of microtubules number per DC phalangeal processes. **G'** Quantification of DC phalangeal processes microtubules density (DC microtubules number per cell cross-section area). Data are presented as mean ± SEM ($n = 3$ samples, three cells per sample were analyzed, unpaired t test, two-tailed). *** denotes a significance level of $P < 0.001$; ns not significant. IHC inner hair cell, IPC inner pillar cell, OPC outer pillar cell, OHC outer hair cell, DC Deiters' cell.
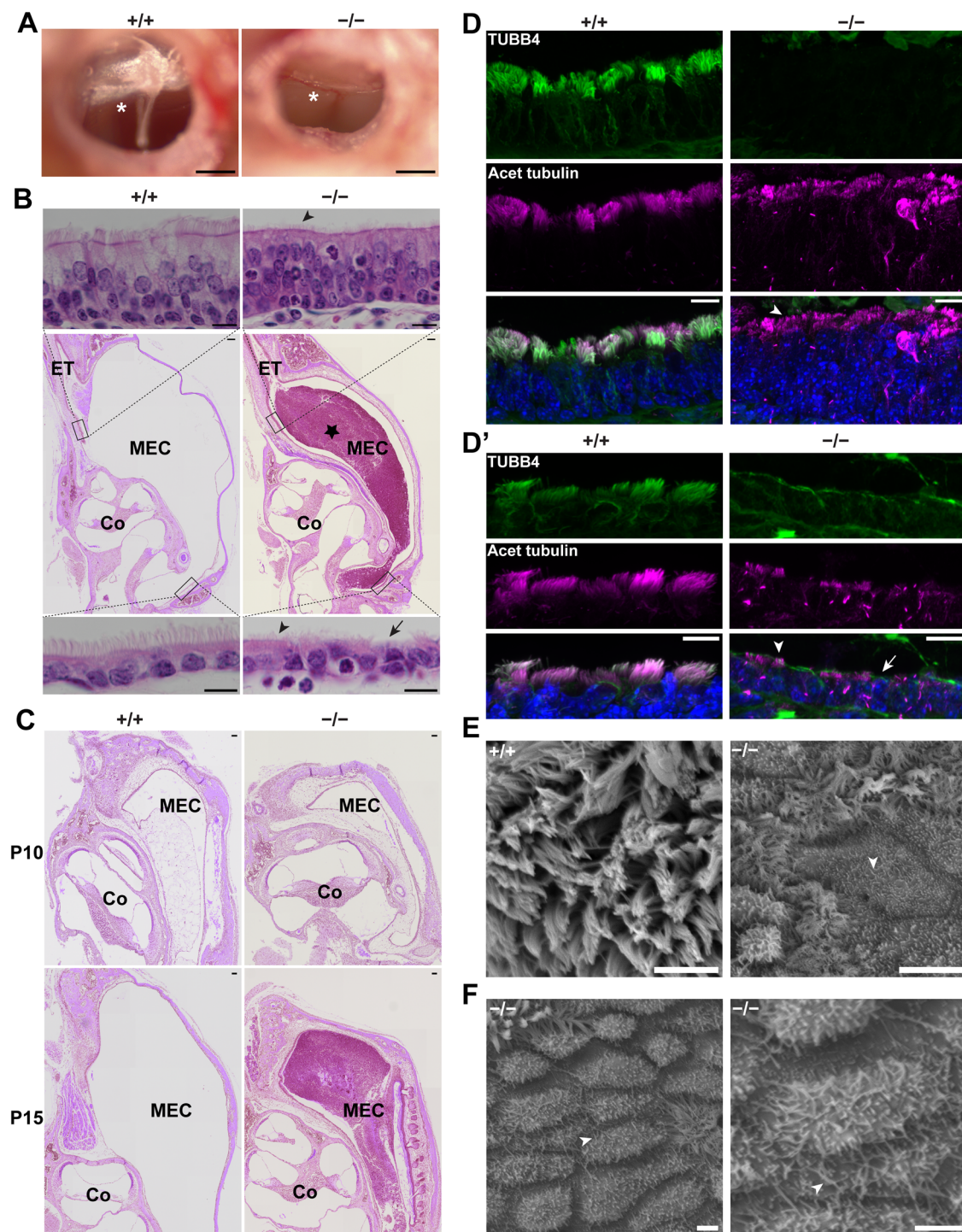
Fig. 6 | Otitis media, and alterations in motile cilia in the absence of TUBB4B.
A Images of the tympanic membrane from 1-month-old *Tubb4b*$^{-/-}$ and control littermate. Scale bar = 0.5 mm. The tympanic membrane is denoted with an asterisk. **B** Cross-section of auditory bullae from 1-month-old *Tubb4b*$^{-/-}$ and control littermate, stained with Hematoxylin and Eosin (H&E). Scale bar = 100 μm. Top panel: Magnified view of ciliated middle ear epithelium near Eustachian tube (ET). Scale bar = 10 μm. Bottom panel: Magnified view of ciliated middle ear epithelium in the dorsal region of the middle ear cavity (MEC). Scale bar = 10 μm. Black arrowheads point to the shortened cilia; black arrow points to the cells missing cilia in the *Tubb4b*$^{-/-}$ middle ear. Effusion in the MEC is marked with a black star. **C** Cross-section of auditory bullae at P10 (top) and P15 (bottom) from *Tubb4b*$^{-/-}$ and control littermate, stained with H&E. Scale bar = 50 μm. **D** Ciliated middle ear epithelium

near ET stained with TUBB4 (green) and acetylated tubulin (magenta, cilia marker) antibodies and DAPI. White arrowheads point to the shortened cilia in the *Tubb4b*$^{-/-}$ middle ear. Scale bar = 10 μm. **D'** Ciliated middle ear epithelium in the dorsal region of the MEC stained with TUBB4 (green) and acetylated tubulin (magenta) antibodies and DAPI (blue). White arrowheads point to the shortened cilia; white arrow points to the cells missing cilia in the *Tubb4b*$^{-/-}$ middle ear. Scale bar = 10 μm. **E** Scanning electron microscopy (SEM) of the middle ear near the ET from P10 *Tubb4b*$^{-/-}$ and control littermates. White arrowheads point to the shortened cilia in the *Tubb4b*$^{-/-}$ middle ear. Scale bar = 5 μm. **F** Magnified SEM view of ciliated cells in the middle ear of *Tubb4b*$^{-/-}$ at P10. White arrowheads point to the shortened cilia in *Tubb4b*$^{-/-}$ middle ear. Scale bar = 2 μm. ET Eustachian tube, MEC middle ear cavity, Co cochlea.
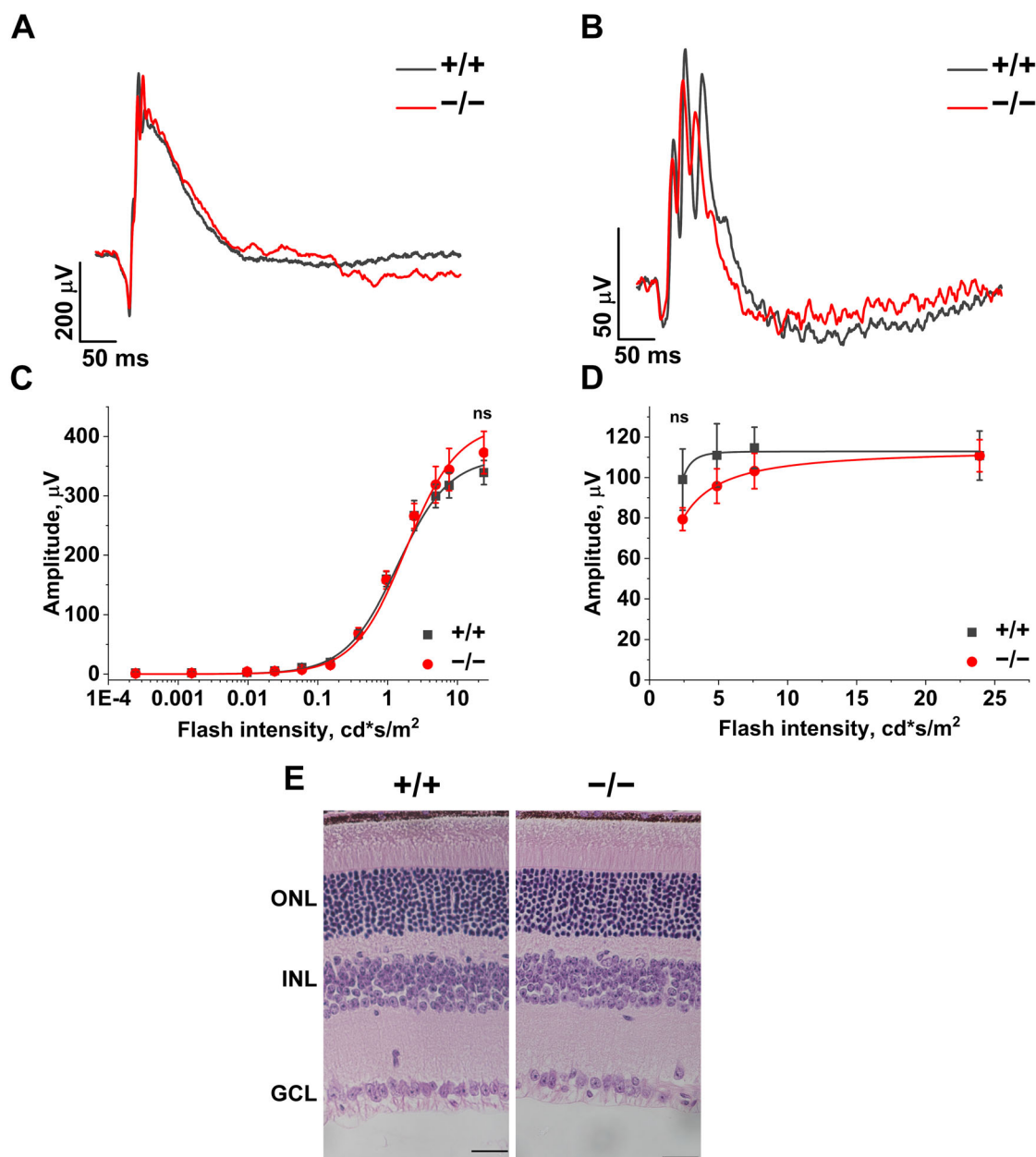
Fig. 7 | TUBB4B is not essential for vision in mice. A Representative scotopic (rod) ERG responses in *Tubb4b*$^{-/-}$ mice (red) and *Tubb4b*$^{+/+}$ littermates (black) at P126. Flash intensity = 0.059 cd*s/m^2. **B** Representative photopic (cone) ERG responses in *Tubb4b*$^{-/-}$ mice (red) and *Tubb4b*$^{+/+}$ littermates (black) at P126. Flash intensity = 23.9 cd*s/m^2. **C** Flash intensity-response relationships for scotopic (rod) a-waves, recorded from P50 to P150. *Tubb4b*$^{+/+}$ is shown in black ($n = 5$) and *Tubb4b*$^{-/-}$ is in red ($n = 10$). The dose-response relationship was fitted with the Hill equation, with maximum amplitudes determined as 364 ± 32 and 420 ± 88 μV for +/+ and −/−, respectively. Statistical analysis performed using two-way ANOVA with a post hoc Tukey test showed no significant differences (ns). **D** Flash intensity-response relationships for photopic (cones) b-waves, recorded from P50 to P150. Tubb4b +/+ is shown in black ($n = 5$) and *Tubb4b*$^{-/-}$ is in red ($n = 10$). The dose-response relationship was fitted with the Hill equation, with maximum amplitudes determined as 113 ± 2, 114 ± 1 μV for +/+ and −/−, respectively. Statistical analysis was performed using two-way ANOVA with a post hoc Tukey test, which showed no significant differences (ns). **E** Retinal cross-sections from 6-month-old *Tubb4b*$^{+/+}$ and *Tubb4b*$^{-/-}$ littermates, stained with hematoxylin and eosin (H&E) stain. Scale bar = 25 μm. Data are presented as mean ± SEM. GCL ganglion cell layer, INL inner nuclear layer, ONL outer nuclear layer.

TUBB6 is upregulated in retinas lacking TUBB4B

The lack of TUBB4B in mice did not result in apparent changes in retinal morphology or function, suggesting that either TUBB4B is dispensable, or a compensatory mechanism is present in the retina. To explore the latter, we measured the transcript levels of other β-tubulin isotypes in the retina from *Tubb4b*$^{-/-}$ and wildtype littermates by reverse transcription quantitative real-time PCR (RT-qPCR). We did not measure *Tubb1* levels as it is not expressed in murine photoreceptor cells[40]. RT-qPCR analysis of β-tubulin isotypes revealed a significant increase of *Tubb6* levels in the retinas lacking β4B-tubulin (*P* value = 0.03) (Fig. 8A), while the mRNA levels of other β-tubulin isotypes in *Tubb4b*$^{-/-}$ retina were comparable to controls. This finding suggested a possible compensatory role for *Tubb6* in mice lacking TUBB4B. We confirmed the increase of β6-tubulin (TUBB6) at the protein level by immunoblotting, using β-tubulin isotype-specific antibodies[31,41]. As expected, TUBB6 protein levels were significantly upregulated in the *Tubb4b*$^{-/-}$ retina by comparison with *Tubb4b*$^{+/+}$ controls (*P* value = 0.01) (Fig. 8B, C). Furthermore, immunofluorescence staining of retinal cross-sections with a TUBB6 antibody showed a robust increase in TUBB6 levels
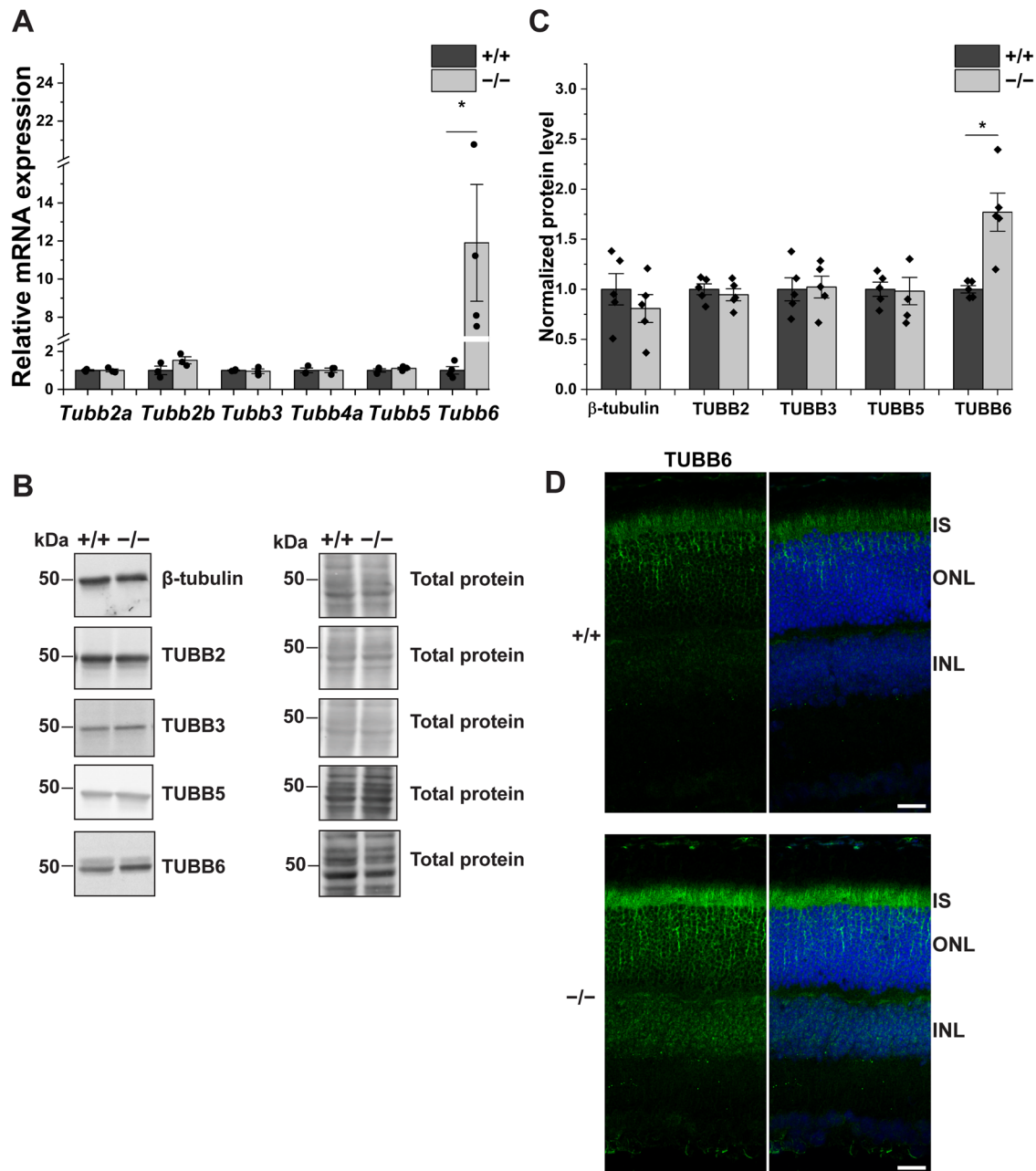
Fig. 8 | Upregulation of TUBB6 in *Tubb4b*^{-/-} murine retina. A Relative mRNA levels of β-tubulin isotypes in retinal tissues from 1-month-old *Tubb4b*^{+/+} and *Tubb4b*^{-/-} mice, assessed by RT-qPCR. Data are presented as mean ± SEM (*n* = 3–4, unpaired *t* test, two-tailed). *P value ≤ 0.05. **B** Immunoblot analysis of β-tubulin isotype protein levels in retinal tissues from 1-month-old *Tubb4b*^{-/-} and wildtype littermates. Antibodies used include pan-β-tubulin, TUBB2, TUBB3, TUBB5, and TUBB6-tubulin (left panel). Total protein stain of corresponding membranes is shown in the right panel (n = 5). **C** Quantification of β-tubulin isotype protein levels from (**B**), normalized to total protein. Data are presented as mean ± SEM (*n* = 5, unpaired *t* test, two-tailed). *P value ≤ 0.05. **D** Retinal cross-sections from *Tubb4b*^{+/+} and *Tubb4b*^{-/-} littermates at 1.5 months, probed with TUBB6 (green) antibody and counterstained with DAPI (blue) for nuclei. Scale bar = 25 μm. ONL outer nuclear layer, INL inner nuclear layer, IS inner segment.

throughout the whole retina of *Tubb4b*^{-/-} mice, including photoreceptor cells (Fig. 8D). Altogether, our findings suggest that a compensatory upregulation of β6-tubulin could mitigate the effects of TUBB4B loss in the retina.

TUBB4B is differentially expressed in primate vs. mouse retina

The *TUBB4B* mutations associated with LCA in humans are heterozygous missense mutations[6,9,18–20]. To further investigate the molecular mechanism behind blindness linked to *TUBB4B* missense mutations in humans, we generated TUBB4B R391C and R391H knock-in mouse models (Fig. S5A, B, C). However, we encountered significant challenges in breeding R391H and R391C colonies beyond the founder mouse (F0 generation) and F1

generation, respectively. The homozygous R391H and heterozygous R391C male mice were sterile and did not produce offspring. Despite the limitations, we performed ERG to assess photoreceptor function in these mice. The ERG responses, scotopic (rods) and photopic (cones), were unaffected even in the older R391H homozygous founder mouse and R391C heterozygous F1 generation knock-in mice, similar to the *Tubb4b*^{-/-} mouse model (Fig. S5 D, E). This finding contrasts with studies in humans where LCA is diagnosed by the absence or diminished ERG response to light stimuli in younger patients[38,39]. Overall, our results show that *Tubb4b* knock-in murine models do not recapitulate blindness linked to *TUBB4B* missense mutations in humans.

Fig. 9 | Species-specific differences in TUBB4B expression in mouse and non-human primate retina. A Retinal cross-sections from 1-month-old *Tubb4b*^{+/+} and *Tubb4b*^{−/−} littermates probed with TUBB4 (green), PRPH2 (magenta) antibodies along with a DAPI nuclear counterstain (gray). **B** Non-human primate retinal cross-sections were probed with TUBB4 (green), PRPH2 (magenta) antibodies, and DAPI (gray). Scale bar = 50 μm. OS outer segment, IS inner segment, ONL outer nuclear layer, OPL outer plexiform layer, INL inner nuclear layer, GCL ganglion cell layer.
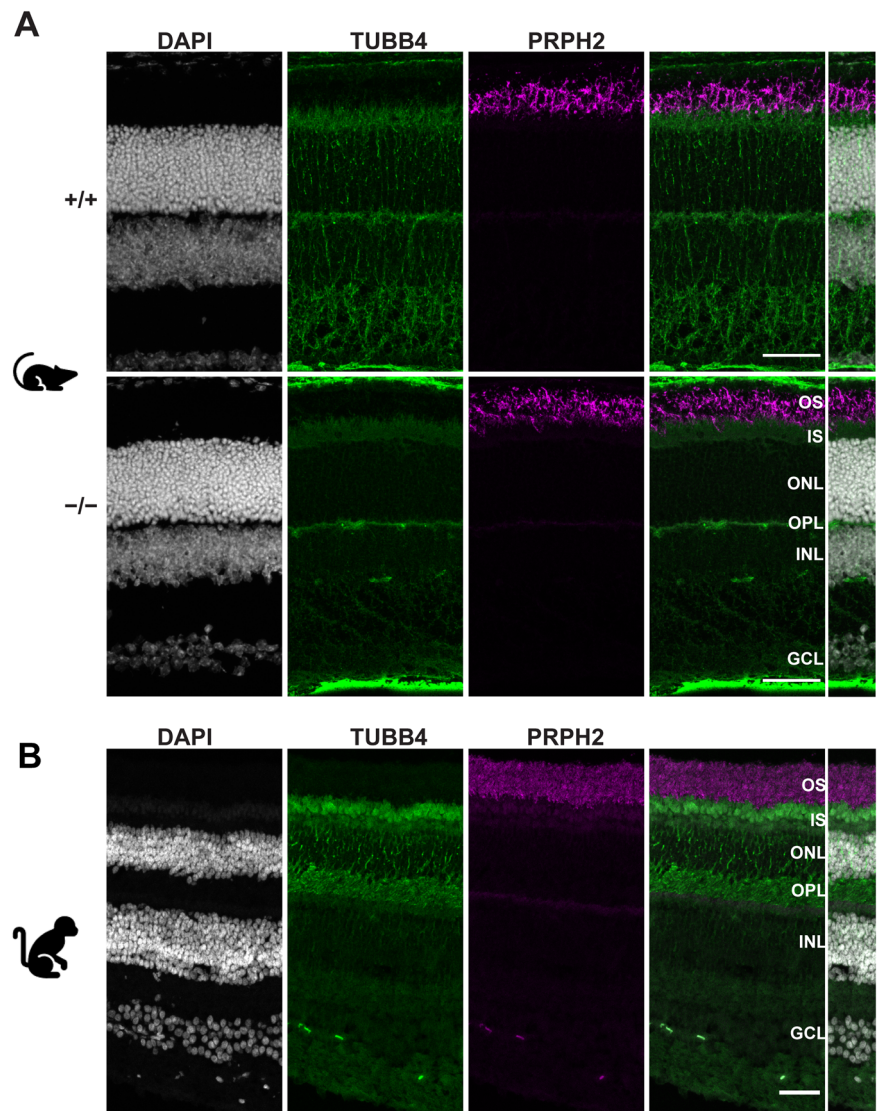
Next, we investigated whether TUBB4B is differentially expressed across species, specifically in rodents and primates. Immunofluorescence staining of murine and non-human primate retinal cross-sections with β4-tubulin antibody revealed species-specific patterns of TUBB4 expression. In the mouse retina, TUBB4 is found throughout the retina (Fig. 9A), while in the non-human primate retina, TUBB4 is specifically expressed in photoreceptors and primarily localized to the inner segment and synaptic region (Fig. 9B). Although the TUBB4 antibody cannot distinguish between TUBB4A and TUBB4B isotypes, considering the high expression of *TUBB4B* in rods[42], we conclude that immunofluorescence staining of non-human primate retina cross-sections predominantly reflects TUBB4B localization.

Discussion

In this study, we investigated the functional role of the β4B-tubulin isotype in hearing and vision. Mice lacking TUBB4B were profoundly deaf, with ultrastructural defects in cochlear supporting cells and ciliary defects in the middle ear, leading to otitis media with effusion (Fig. 10). The absence of TUBB4B did not lead to hair cell degeneration or apparent defects in cochlear sensory cells. Although mutations in *TUBB4B* are associated with severe blinding diseases in humans, mice lacking β4B-tubulin and knock-in mouse models expressing disease-linked mutations did not exhibit any visual impairments. Our findings indicate a species-specific discrepancy in

the expression of tubulin isotypes and compensation by other tubulin isotypes in the mouse retina.

Microtubules are the dominant cytoskeletal filaments defining the mechanical properties of supporting cells, allowing them to withstand deformation occurring when a sound wave travels through the cochlea[26]. The length and number of microtubules define the mechanical properties of outer pillar cells[26,43]. Indeed, incubation of cochlear explant cultures with nocodazole, which induces microtubule depolymerization, decreased pillar cell stiffness, measured by Young's modulus, demonstrating the importance of intact microtubules to the mechanical properties of pillar cells[27]. In contrast, disruption of the actin network did not affect the stiffness of pillar cells[27]. A recent study demonstrated that mice lacking GAS2, a microtubule-associated protein, develop hearing loss[28]. Defective hearing in GAS2 animals is attributed to microtubule bundle disorganization and reduced microtubule number in supporting cells, decreasing the stiffness of the pillar and Deiters' cells and affecting cochlear mechanics[28]. Moreover, humans with mutations in *GAS2* developed hearing loss, highlighting the importance of microtubule bundle integrity in hearing[28]. Based on the decreased microtubule number and microtubule disorganization in pillar cells of *Tubb4b*^{−/−} mice observed in this study, we propose that the mechanical properties of pillar cells are similarly reduced in mice lacking TUBB4B.

The absence of TUBB4B did not result in a dramatic change in microtubule density in the phalangeal processes of Deiters' cells. However, it
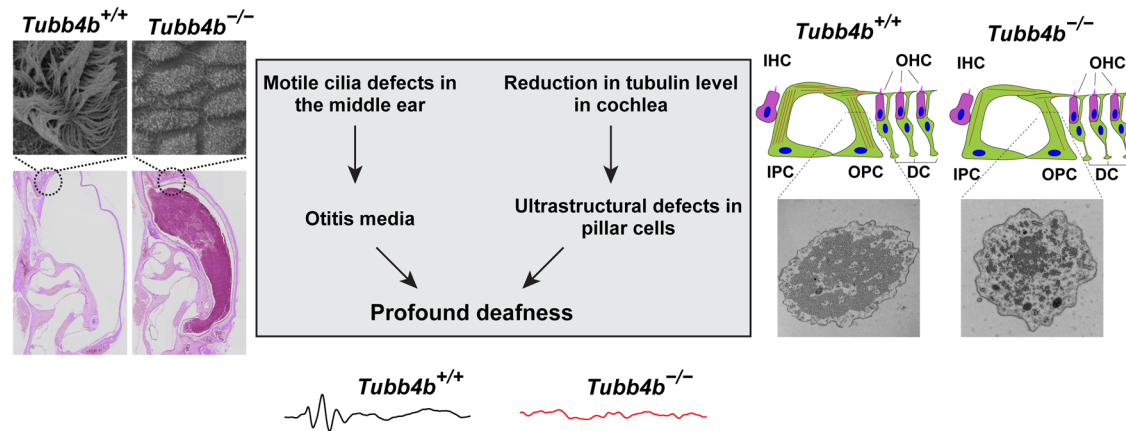
Fig. 10 | Summary of role for TUBB4B in hearing. *Tubb4b* knockout mice are profoundly deaf due to defects in both middle and inner ear (middle panel). In the middle ear, lack of TUBB4B leads to defective motile cilia causing otitis media, indicating an essential role for TUBB4B in motile cilia development and/or maintenance (left panel). In the inner ear, TUBB4B deficiency results in disorganized and reduced microtubules in pillar cells, suggesting a critical role for TUBB4B in providing mechanical support for auditory transmission through the cochlea (right panel).

is plausible that microtubule density could be affected in the basal region of Deiters' cells in mice lacking β4B-tubulin. Indeed, immunostaining of cochlear whole mounts revealed significantly narrower microtubule stalks in *Tubb4b*^{−/−} mice (Fig. 4E, F). Furthermore, we also noted a decrease in the diameter of phalangeal processes in the basal turn of the organ of Corti but not in the apical or middle turns (Fig. S4B). It is worth noting that we used apical-middle cochlear turns for the TEM studies. Therefore, it is possible that microtubule number in the phalangeal processes of Deiters' cells in the basal turn of Organ of Corti could be affected in the absence of TUBB4B, and future studies using TEM would be needed to quantify the microtubule density in Deiters' cells along the cochlear turns.

Analysis of single-cell RNA sequencing (scRNA-seq) data of the murine cochlear epithelium from a previously published paper[44], revealed that Deiters' cells β-tubulin transcripts are equally distributed among *Tubb2a*, *Tubb2b* and *Tubb4b* isotypes (Fig. S6). It is plausible that TUBB2 isotypes may compensate for the loss of TUBB4B in Deiters' cells and maintain microtubule density in phalangeal processes. Indeed, RT-qPCR analysis of cochlear extracts suggests a trend towards an increase in both *Tubb2a* and *Tubb2b* transcripts in mice lacking β4B-tubulin (Fig. S7). In contrast, *Tubb4b* is a predominant β-tubulin isotype in both inner and outer pillar cells (Fig. S6). Therefore, a decrease in microtubule density in these cells can be attributed to the inability of other β-tubulin isotypes to compensate for the loss of the TUBB4B in pillar cells.

To our knowledge, pillar cells are the only mammalian cells with 15-protofilament microtubules, instead of typical 13-protofilaments[45–47]. In *C. elegans*, 15-protofilament microtubules are found in touch receptor neurons. In the absence of MEC-12 (α-tubulin isotype) or MEC-7 (β-tubulin isotype) or MEC-17 and its paralog ATAT-2 (α-tubulin acetyltransferases) 15-protofilament microtubules are not formed, suggesting that certain α-, β-tubulin isotypes and tubulin post-translational modifications can specify microtubules protofilament number[48–50]. Interestingly, in the absence of α-tubulin acetyltransferase, ATAT1, in mice, the formation of 15-protofilament microtubules in pillar cells is unaffected[47], suggesting that the tubulin isotypes could be another mechanism of microtubule protofilament number regulation in vertebrates. Indeed, an in vitro study using isotypically pure recombinant human tubulin demonstrated that β-tubulin isotypes could determine microtubule protofilament number[51]. Taken altogether, it is plausible that TUBB4B may facilitate the formation of 15-protofilament microtubules in pillar cells, given a high *Tubb4b* transcript expression level relative to other tubulin isotypes (Fig. S4). However, future TEM studies focusing on microtubule protofilament numbers in pillar cells using *Tubb4b*^{−/−} mice are needed to test this conjecture.

Mutations in *TUBB4B* are linked with primary ciliary dyskinesia (PCD)[9], a disease caused by motile cilia dysfunction. Immunostaining of various tissues demonstrated the presence of β4-tubulin (TUBB4) in motile cilia of the trachea, brain ependyma, fallopian tube, and efferent ducts in testes, suggesting a specialized role for TUBB4 in motile cilia[23]. Intriguingly, recent studies demonstrated the need for TUBB4B in motile cilia assembly, integrity of cilia, and ciliary axonemes in airway epithelial cells[9,24]. It is worth noting that *Tubb4a; Tubb4b* double knockout mice did not exhibit exacerbated ciliary defects, indicating a distinct functional role for TUBB4B in motile cilia[24]. Furthermore, mice lacking TUBB4B displayed hydrocephaly and did not survive beyond P40[9,24]. *Tubb4b*^{−/−} mouse model described in this study also showed airway ciliary defects (Fig. S8), varying degrees of hydrocephaly, and lethality with age. However, our *Tubbb4b*^{−/−} mice survived beyond P40, possibly due to differences in mouse genetic background.

Moreover, some PCD patients carrying *TUBB4B* mutations have conductive hearing loss. Chronic otitis media with effusion causes conductive hearing loss, a condition linked to defects in motile cilia[52]. The middle ear cavity is lined with epithelium comprised of multiciliated and non-ciliated cells. The movement of motile cilia assists in removing contaminants from the middle ear cavity into the nasopharynx through the Eustachian tube. Previous studies demonstrated the presence of dual populations of multiciliated cells in the mouse middle ear epithelium, near the Eustachian tube, and in the dorsal region of the middle ear, distinct in their origin[52]. Mouse models with defects in motile cilia, such as *Mdnah5*^{−/−} or Spag6^{−/−} mutant mice, develop otitis media with effusion[53,54]. Here, we show that the absence of TUBB4B resulted in defective motile cilia in the middle ear. Our immunofluorescence staining of auditory bullae cross-sections showed TUBB4B localization to motile cilia in both populations of multiciliated cells in the middle ear, and the lack of TUBB4B resulted in shorter cilia and cilia density reduction in both populations. Given the importance of TUBB4B in motile cilia assembly of airway epithelial cells[9,24], its absence likely leads to defective multiciliogenesis in the middle ear, contributing to the otitis media with effusion that was present as early as P15 in *Tubb4b*^{−/−} mice. Altogether, these results contribute to the body of knowledge on the importance of TUBB4B in motile cilia, specifically in the middle ear.

Our study demonstrates that *Tubb4b*^{−/−} mice are profoundly deaf, caused by defects in both middle and inner ears (Fig. 10). Indeed, middle ear defects, such as otitis media, can impair sound transfer to the inner ear and lead to elevated ABR and DPOAE thresholds[55]. Furthermore, a decrease in microtubule density in pillar and Deiters' cells in the inner ear results in elevated ABR thresholds and reduced DPOAEs[28]. Although the DPOAE reduction is often due to OHC dysfunction, the reduced stiffness of cochlear supporting cells can also impair the ability of OHCs to withstand mechanical stress and/or can affect OHCs electromotility. The lack of TUBB4B did not lead to apparent defects in cochlear sensory cells, and the

stereocilia bundle was indistinguishable between control and mutant mice assessed by high-resolution confocal microscopy as well as SEM. Unfortunately, the contributions of middle or inner ear phenotypes to deafness displayed by mice lacking TUBB4B are unclear. Therefore, future studies using conditional $Tubb4b^{-/-}$ models will be needed to address this knowledge gap. Moreover, it will be necessary to model specific disease-causing TUBB4B variants to provide additional insights into the pathophysiology behind sensorineural hearing loss.

β4B-tubulin is not essential for photoreceptor function and development in mice. The absence of a vision phenotype in the murine model for TUBB4B deficiency is likely due to the compensatory effects and functional redundancy among β-tubulin isotypes. Indeed, previous analysis of $Tubb2a^{-/-}$, $Tubb2b^{-/-}$, $Tubb3^{-/-}$ and $Tubb4a^{-/-}$ murine models indicated that total β-tubulin levels in the mutants were unaltered[17,56,57]. In the $Tubb4a$ knockout animal model, an equivalent level of total β-tubulin was achieved by transcriptional upregulation of $Tubb2a$, $Tubb2b$, and $Tubb5$[17]. In the $Tubb3$ knockout model, subtle (10–20%) increases in other β-tubulin isotype transcripts compensated for the loss of TUBB3[57]. Similarly, our study found that the total β-tubulin protein levels were unaltered in the $Tubb4b^{-/-}$ retina. Moreover, there was a marked increase in $Tubb6$ mRNA level and β6-tubulin protein levels in the knockout retina, showing compensatory upregulation within the β-tubulin family in the outer and inner retina in the absence of TUBB4B.

The $Tubb4b^{+/R391C}$ and $Tubb4b^{R391H/R391H}$ knock-in mouse models that mimic the LCA mutations found in humans exhibited normal retinal function. Furthermore, our immunofluorescence analysis of TUBB4 expression in the monkey and murine retina indicates that the lack of visual impairment in the knockout and knock-in mouse models is likely due to the differential expression of TUBB4B across the species. Indeed, a recent study identified differences in gene expression between human and mouse retinal development, and $TUBB4B$ was one of the genes differentially expressed in photoreceptor cells[42]. This species-specific difference in TUBB4B expression may explain the discrepancy in the vision phenotype, as observed in other models for retinal diseases. For example, mouse models of Usher syndrome 1, a deafness-blindness disorder, phenocopy hearing loss but fail to recapitulate the defects in retinal structure or function[58,59]. Mutations in MYO7A, a protein localized to calyceal processes of primate photoreceptors, are associated with Ushers syndrome type 1B[60]. In contrast, mouse photoreceptors lack the calyceal processes[60]. Indeed, MYO7A protein is expressed at higher levels in non-human primate photoreceptors than in mouse photoreceptors, suggesting that the absence of retinal degeneration in $Myo7a^{-/-}$ mice is due to differences in photoreceptor structure and differential expression of MYO7A across species[59]. Given the species-specific differences, to better understand the mechanism underlying retinal diseases caused by mutations in the human $TUBB4B$ gene, human retinal organoids or animal models with photoreceptor calyceal processes and similar β4B-tubulin expression patterns as in human photoreceptors should be considered.

This study demonstrates that $Tubb4b^{-/-}$ mouse model faithfully recapitulates hearing loss but not retinal dystrophy resulting from mutations in $TUBB4B$, and thus mouse models are a suitable model to understand the pathophysiology behind sensorineural hearing loss. Furthermore, we propose that TUBB4B has a unique role in motile cilia formation in the middle ear, and TUBB4B is needed to provide supporting cells with mechanical properties to transmit sound through the cochlea.

Methods
Ethics statement
All mice were bred and maintained under a 12 h/12 h light/dark cycle. Food and water were available *ad libitum*. All animals used in this study were handled and housed according to approved Institutional Animal Care and Use Committee (IACUC) protocol # 1803013440 of West Virginia University. We have complied with all relevant ethical regulations for animal use. P4 to P180 mice of both sexes were used in this study.

Animal model and genotyping
$Tubb4b^{-/-}$ murine model in C57BL/6NJ background was obtained from The Jackson Laboratory (Catalog # 43743-JAX). We crossed the animals to 129SV/E strain and maintained them in the mixed background to eliminate the $rd8$ allele[61]. Genotyping for $Tubb4b$ and $rd8$ alleles was performed using primers listed in Table S1. The thermocycling conditions for $Tubb4b$ genotyping were 95 °C for 4 min, 35 cycles of 95 °C for 30 s, 55 °C for 30 s, 72 °C for 30 s, and a final extension step of 72 °C for 5 min.

$Tubb4b$ knock-in mice (R391C and R391H) were generated at the Mouse Transgenic and Gene Targeting Core at Emory University. The guide RNA (gRNA) and repair oligonucleotides used to generate point mutants are listed in Table S2. Genotyping for $Tubb4b$ point mutations was performed using primers listed in Table S1. The thermocycling conditions were 95 °C for 4 min, 38 cycles of 95 °C for 30 s, 60 °C for 30 s, 72 °C for 30 s, and a final extension step of 72 °C for 5 min. The PCR product sequencing was performed by Psomagen Inc.

Electroretinography
Electroretinography (ERG) was performed using the UTAS Visual Diagnostic System (LKC Technologies, Gaithersburg, MD, USA). Mice were dark-adapted overnight before testing. Mice were anesthetized with 2.5% isoflurane for 5 min. The eyes were dilated with a 1:1 mixture of 1% tropicamide ophthalmic solution and 2.5% phenylephrine hydrochloride ophthalmic solution. Mice were then placed on a heated platform with a continuous isoflurane flow through a nose cone (1.5% isoflurane). A drop of GenTeal Tears eye gel (Alcon) was added to each eye, and electrodes were placed on each cornea. The reference electrode was placed into the scalp subcutaneously. Rod responses (scotopic) were obtained in the dark with flashes of LED white light at increasing flash intensities. Cone responses (photopic) were recorded after the animals were light-adapted with a saturating white background light for 10 min.

Immunoblotting
Mice were euthanized by CO_2 inhalation, followed by cervical dislocation; eyes were enucleated for retina collection, and cochleae were extracted from temporal bones. Dissected retinas and cochleae were frozen in dry ice. The retina samples were sonicated in phosphate buffer saline (PBS) containing a protease inhibitor cocktail (Thermo Fisher) and 1 mM dithiothreitol (DTT). The cochlea samples were sonicated in radioimmunoprecipitation assay (RIPA: Research Products International) lysis buffer (50 mM Tris, 150 mM NaCl, 1% NP-40, 0.5% Sodium Deoxycholate, 0.1% SDS) containing protease and phosphatase inhibitor cocktail (Thermo Fisher). Protein concentrations were measured using NanoDrop spectrophotometer or BCA protein assay (Thermo Fisher). An equal amount of proteins (50 μg) from each sample were loaded into individual lanes, separated by SDS-PAGE gel, and transferred onto polyvinylidene difluoride (PVDF) membranes (Immobilon). Then, the membranes were stained for total protein (LI-COR). After blocking with blocking buffer (LI-COR, or Thermo Fisher) for 30 min at room temperature, the membranes were incubated with primary antibodies overnight at 4 °C or 4 h at room temperature. The membranes were washed with PBST (PBS containing 0.1% Tween-20) three times for 5 min each at room temperature. Then, the membranes were incubated with secondary antibodies for 30 min at room temperature and washed with PBST three times for 5 min at room temperature. The membranes were imaged using the Odyssey Infrared (LI-COR) or Amersham Typhoon imaging systems. Quantification of the density of the protein bands was performed using Fiji software. Antibodies used in this study are listed in Table S3.

Immunofluorescence staining of retinal cross-sections
For immunofluorescence staining of murine retinal cross-sections, enucleated eyes were submerged in 4% paraformaldehyde (PFA) in PBS for 30–45 s and then immediately flash frozen in optimal cutting temperature (OCT: Tissue-Tek) compound. 12 μm thick eye cross-sections were cut on

Leica CM1860 cryostat, mounted onto superfrost slides. The retinal cross-sections were incubated in blocking buffer (10% goat serum, 0.5% TritonX-100, and 0.05% (w/v) sodium azide in PBS) for 1 h, followed by a 4-hour incubation with primary antibodies listed in Table S3 at room temperature. The sections were washed with PBS. Next, the slides were incubated with secondary antibodies and DAPI (diamidino-2-phenylindole; Invitrogen) for 1 h at room temperature. Then, the slides were washed with PBS. Slides were mounted with ProLong Gold Antifade reagent (Invitrogen) and coverslipped.

Non-human primate eyes were enucleated and protected from light as much as possible for immunofluorescence staining of monkey retinal cross-sections. A 6 mm biopsy punch was used to create a hole in the cornea, and the globe was placed into a 4% PFA solution overnight. The following morning, the eye was transferred to 0.1 M PBS/0.03% sodium azide solution. Eyes were dissected, and retinas were cryosectioned (10 μm). The retinal cross-sections were incubated in 10 mM citrate buffer, pH = 6.0, at 95 °C to unmask the antigen. Then, the sections were washed with PBS and incubated in a blocking buffer (10% goat sera, 0.5% TritonX-100, 0.05% sodium azide in PBS) for 1 h. Then, the sections were incubated overnight with the primary antibodies listed in Table S3. The sections were washed thrice with PBS containing 0.1% TritonX-100 for 5 min. Next, the slides were incubated with secondary antibodies and DAPI for 1 h at room temperature. Then, the slides were washed two times with PBS containing 0.1% TritonX-100 for 5 min each, followed by a wash with PBS for 5 min. An autofluorescence eliminator (Sigma) was used to reduce autofluorescence. Slides were mounted with ProLong Gold Antifade reagent (Invitrogen) and coverslipped.

Immunofluorescence staining of cochlear wholemounts and cryosections

For immunofluorescence staining of cochlear wholemounts from adult mice, inner ears were dissected in PBS. The stapes was removed from the oval window. A small hole was made in the apex of the cochlea using a 27 G needle, and the cochlea was gently and slowly perfused with 4% PFA via the round and oval windows until the solution was washed out of the small hole at the apex. The inner ears were fixed in 4% PFA in PBS overnight at 4 °C then washed with PBS. Then, the inner ears were decalcified in 120 mM EDTA solution for 3 days at 4 °C, followed by three washes in PBS. The organ of Corti was dissected in PBS as described in ref. 62. Dissected cochlear turns (apical, middle, and basal) were blocked in a blocking buffer for 1 h. The tissues were incubated with primary antibodies overnight at 4 °C, followed by three washes with PBS. Next, the samples were incubated with secondary antibodies for 1 h at room temperature and then washed with PBS. The tissues were mounted onto slides with ProLong Gold Antifade reagent (Invitrogen) and coverslipped.

For immunofluorescence staining of cochlear wholemounts from P4 pups, inner ears were dissected in PBS. The stapes were removed from the oval window. A small hole was made in the apex of the cochlea using forceps and fixed in 4% PFA in PBS for 30 min, then washed with PBS. Dissected organs of Corti were blocked and stained with antibodies in the same fashion as for adult cochlear wholemounts.

For immunofluorescence staining of cochlear cryosections, inner ears from adult mice and pups were fixed and decalcified (for adult mice only) in the same fashion as for wholemounts preparation. Inner ears were incubated in 30% sucrose in PBS overnight at 4 °C. Inner ears were then incubated in a 1:1 mixture of 30% sucrose: OCT for 1 h at 4 °C and flash frozen in OCT. In all, 16 μm thick cochlear cross-sections were cut on Leica CM1860 cryostats, mounted onto superfrost slides, and stored at −20 °C. Immunofluorescence staining of cochlear cross-sections was performed in the same fashion as for cochlear wholemounts.

For immunofluorescence staining of auditory bullae cross-sections, auditory bullae from P10 mice were dissected from temporal bones and fixed in 4% PFA in PBS overnight at 4 °C, followed by PBS washes. Next, the samples were decalcified in 120 mM EDTA solution for 2 h at room temperature. Auditory bullae were incubated in 30% sucrose in PBS overnight at

4 °C. Inner ears were then incubated in a 1:1 mixture of 30% sucrose: OCT for 1 h at 4 °C and flash frozen in OCT. In all, 16 μm thick sections were cut on Leica CM1860 cryostats, mounted onto superfrost slides, and stored at −20 °C. Immunofluorescence staining of auditory bullae cross-sections was performed in the same fashion as for cochlear wholemounts.

For immunofluorescence staining of inner hair cell synapses, the cochlea was gently and slowly perfused with 2% PFA via the round and oval windows until the solution was washed out of the small hole at the apex. The inner ears were fixed for 15 min in 2% PFA, the cochlear bones were carefully peeled out using a 27 G needle, and the apical turn of the organ of Corti was dissected. The dissected apical turn of the organ of Corti was blocked and stained with antibodies in the same fashion as for adult cochlear wholemounts.

Confocal microscopy
Confocal imaging was performed with a Nikon C2 confocal microscope with Plan fluor 40×/1.30 NA oil, Plan Apo λ 60×/1.40 NA oil, or Plan Apo λ 100×/1.45 NA oil objectives, Nikon Crest V3 spinning disk confocal microscope with Plan Apo λD 20×/0.80 NA or Plan Apo λD 60×/1.42 NA oil objectives, or Zeiss 710 confocal microscope with Airyscan Super Resolution with Plan Apochromat 63×/1.40 NA oil objective. All images represent maximum intensity projections of z-stack generated using Nikon NIS-Elements or Fiji software.

FM1-43FX dye uptake
Organs of Corti from P7 pups were dissected in Hanks' Balanced Salt Solution (HBSS) (Gibco) containing 1.3 mM Ca^{2+}. The tissues were incubated in 6 μM FM1-43FX (Invitrogen) in HBSS with calcium for 30 s and washed three times with HBSS with calcium for 2 min each. Next, the organs of Corti were fixed in 4% PFA for 30 min and stained with phalloidin.

ABR and DPOAE
Acoustic sound stimuli were calibrated in the open-field configuration with a pre-amp (Type 2690-0S1, Brüel and Kjær) attached microphone (1/4 inch 4954-B, Brüel and Kjær) and a reference 1 kHz, 94 dB SPL calibrated sound source (Type 4230, Brüel and Kjær). We placed the microphone in the same position as the mouse ear, delivered the broadband click stimuli at a specific voltage input, and recorded output voltage using the pre-amp microphone. We then determined the voltage input needed to generate the desired dB SPL output from a speaker (MF1, Tucker–Davis Technologies) using the 1 kHz 94 dB SPL calibrated sound source as the reference.

Auditory brainstem response (ABR) measurements were conducted in a sound-attenuating chamber (env-022s, Med Associates inc.) and taken in the open-field configuration, with the speaker placed 10 cm from the right ear of the mouse. Experiments were performed with mice under isoflurane anesthesia (3% induction/1.5% maintenance, in oxygen) and kept at a stable temperature (~37 °C) with a heat pad. ABR thresholds were measured with subdermal electrodes in 1-month-old mice using the RZ6 processor (Tucker–Davis Technologies). Subdermal electrodes were placed at the vertex of the skull (recording), ventral to the left pinna (ground), and ventral to the right pinna (reference). ABR measurements were recorded with BioSigRX software during the presentation of broadband clicks (10 ms duration, 0–90 dB SPL in 10 dB steps) at a rate of 21 per second with a calibrated MF1 speaker (Tucker–Davis Technologies) in open-field configuration. We presented each sound 512 times and analyzed the average evoked potential after bandpass filtering the waveform between 100 and 3000 Hz. ABR threshold was defined as the lowest sound intensity that generated ABR wave I amplitudes. ABR wave I amplitudes were identified as the first consistently generated wave with decreased amplitudes and latency as stimulus intensity (in dB SPL) decreased. Baseline noise levels were measured using the pre-stimulus baseline for each animal. All experiments were performed blind to genotype.

Distortion product otoacoustic emission (DPOAE) measurements were recorded in a sound-attenuating chamber as above. One-month-old mice were anesthetized using isoflurane and kept at a stable temperature

(~37 °C) as above. DPOAE measurements were taken with the RZ6 processor and BioSigRX software (Tucker–Davis Technologies). Tone pairs were presented with an f1 and f2 primary ratio of 1.2. The f1 and f2 primaries were presented using two separate MF1 speakers (Tucker–Davis Technologies). Each speaker presented one tone frequency into the outer ear canal via tubing that came together within an acoustic probe inserted into the ear canal. The presentation of these two tones results in the generation of DPOAEs, which were recorded with a microphone (ER-10B, Etymotic). Sound pairs had a center frequency of 16 kHz and were presented at intensities from 20 to 80 dB SPL in 10 dB steps. Each intensity was averaged over 512 sweeps.

Hematoxylin and eosin staining
Mice were euthanized, enucleated eyes, and dissected auditory bullae were fixed in Excalibur's Alcoholic z-fix (Excalibur Pathology Inc., Norman, OK). Auditory bullae were decalcified in 5% formic acid for 1 day. The samples were cross-sectioned and stained with hematoxylin and eosin (H&E) by Excalibur Pathology Inc. Images of sections stained with H&E were taken with a Nikon Eclipse Ti microscope with DS-Ri2 camera with Plan fluor 40×/1.30 NA oil or Plan Apo λ 100×/1.45 NA oil objectives or Olympus VS120 Slide Scanner with Plan S Apo 10×/0.40 NA, U Plan S Apo 20×/0.75 NA or U Plan S Apo 40×/0.95 NA objectives.

Scanning electron microscopy (SEM)
The auditory bullae from P10 pups were dissected and fixed in 2.5% glutaraldehyde in 0.1 M cacodylate buffer (pH=7.2) containing 2 mM $CaCl_2$. After three washes in 0.1 M cacodylate buffer, middle ear cavities were dissected and post-fixed in an aqueous solution of 1% OsO_4 for 1 h in dark. Next, the samples were washed in water thrice for 15 min each. The samples were dehydrated in a graded ethanol series (30%, 50%, 70%, 90%, 95%, 100%, 100%) for 15 min each. Next, the samples were incubated in hexamethyldisilazane (HMDS) for 15 min and air-dried overnight. The samples were mounted and sputter coated with gold/palladium using Denton Desk V Sputter. The auditory bullae were examined with a JEOL JSM 7600 F scanning electron microscope at 8 kV.

The inner ears of 1-month-old mice were dissected in Leibovitz's L-15 Medium. The stapes were removed from the oval window. A small hole was made in the apex of the cochlea using a 27 G needle, and the cochlea was gently and slowly perfused with a solution of 1% glutaraldehyde/4% PFA in 0.1 M cacodylate buffer containing 2 mM calcium chloride ($CaCl_2$) via the round and oval windows until the solution was washed out of the small hole at the apex. Then, the samples were prefixed in 1% glutaraldehyde/4% PFA in 0.1 M cacodylate buffer supplemented with 2 mM calcium chloride for 1 h at room temperature, followed by fixation in 2.5% glutaraldehyde in 0.1 M cacodylate buffer containing 2 mM $CaCl_2$. After three washes in 0.1 M cacodylate buffer, the samples were incubated in 0.25 M EDTA for 3 days at 4 °C. After three washes in distilled water, the organ of Corti was dissected in water. The sample post-fixation, dehydration, drying, and sputtering were performed in the same fashion as for middle ear SEM. The organ of Corti was examined with a JEOL JSM 7600 F scanning electron microscope at 4 kV.

Transmission electron microscopy (TEM)
The inner ears of 1-month-old mice were dissected in Leibovitz's L-15 media (Gibco, 21083027). The stapes were removed from the oval window, and a small hole was made in the apex of the cochlea. The cochlea was gently and slowly perfused with fixative via the round and oval windows and fixed in 2.5% glutaraldehyde in 0.1 M cacodylate buffer (pH = 7.2). After three washes in 0.1 M cacodylate buffer, the samples were incubated in 4% tannic acid solution in 0.1 M cacodylate buffer for 1 h at room temperature. Next, the samples were washed with cacodylate buffer and decalcified in 0.25 M EDTA solution in 0.1 M cacodylate buffer overnight at 4 °C, followed by washes in cacodylate buffer. The cochlear turns were dissected and post-fixed in 2% osmium tetroxide in 0.1 M cacodylate buffer for 1 h on ice. The samples were washed in water (four times), followed by overnight

incubation in 1% uranyl acetate. The organ of Corti samples were dehydrated in a graded ethanol series (30%, 50%, 70%, 95%) for 10 min each on ice, followed by incubation in 100% twice for 15 min each at room temperature. Dehydrated organs of corti were then washed in propylene oxide twice, followed by incubation in a series of propylene oxide and resin mix as follows: 50%:50% (2 h), 25%:75% (overnight), and 100% resin twice at room temperature (2 h). Resin-embedded sections were then mounted in silicone EM molds and cured at a 60 °C oven overnight. Ultrathin resin sections of 70 nm were cut using Leica UC7 ultramicrotome with a Diatome diamond knife. Ultrathin sections were collected onto grids and stained with 3% lead citrate stain for 2 min. After the staining step, the grids were rinsed in filtered water and dried. TEM imaging was performed on a JEOL JEM-1010.

RNA extraction and RT-qPCR
For the reverse transcription PCR, dissected retinas from 1-month-old mice were collected in 200 μL of TRIzol and frozen in dry ice. RNA was extracted using an RNA purification kit (Invitrogen) with on-column DNase treatment (Invitrogen) according to the manufacturer's recommendations. Eluted RNA was used for cDNA synthesis using SuperScript IV VILO Master Mix (Invitrogen). For qPCR, 5 ng of cDNA was added to a mixture containing 250 nM of forward and 250 nM of reverse primers and SYBR Green qPCR Master Mix (Agilent Technologies). Yhwaz, Polr2b, and Atp5b were used as reference genes. The PCR amplification efficiencies for each primer set were confirmed to be between 90% and 110%. ΔΔCt method with the inclusion of primer efficiencies for the reference and target genes was used to analyze qPCR data[63,64]. qPCR was performed on Stratagene MX3000p or Bio-Rad CFX96 cyclers. Primer sequences are listed in Table S4.

Statistics and reproducibility
Statistical analyses were performed in OriginPro software. All data are represented as mean ± standard error of the mean. All data are a representation of a minimum of three independent experiments. Two-way ANOVA with post hoc Tukey test was used to analyze scotopic and photopic ERG responses from $Tubb4b^{-/-}$ and control mice at different light intensities. An unpaired t test (two-tailed) or Mann–Whitney U test were used to compare measured values between control and $Tubb4b^{-/-}$ samples. Mendelian ratios were analyzed using the Chi-square test with 2 degrees of freedom.

Reporting summary
Further information on research design is available in the Nature Portfolio Reporting Summary linked to this article.

Data availability
All data supporting of this study are available within the paper and its supplementary information. Supplementary Data 1 represents the numerical source data for graphs Figs. 1, 3, 4, 5, 7 and 8.

References
1. Goodson, H. V. & Jonasson, E. M. Microtubules and microtubule-associated proteins. *Cold Spring Harb. Perspect. Biol.* https://doi.org/10.1101/cshperspect.a022608 (2018).
2. Barlan, K. & Gelfand, V. I. Microtubule-based transport and the distribution, tethering, and organization of organelles. *Cold Spring Harbor. Perspect. Biol.* https://doi.org/10.1101/cshperspect.a025817 (2017).
3. Janke, C. & Magiera, M. M. The tubulin code and its role in controlling microtubule properties and functions. *Nat. Rev. Mol. Cell Biol.* **21**, 307–326 (2020).
4. Roll-Mecak, A. The tubulin code in microtubule dynamics and information encoding. *Dev. Cell* **54**, 7–20 (2020).

5. Breuss, M. et al. Mutations in the β-tubulin gene TUBB5 cause microcephaly with structural brain abnormalities. *Cell Rep.* **2**, 1554–1562 (2012).

6. Luscan, R. et al. Mutations in TUBB4B cause a distinctive sensorineural disease. *Am. J. Hum. Genet.* **101**, 1006–1012 (2017).

7. Feng, R. et al. Mutations in TUBB8 and human oocyte meiotic arrest. *New Engl. J. Med.* **374**, 223–232 (2016).

8. Bahi-Buisson, N. et al. The wide spectrum of tubulinopathies: what are the key features for the diagnosis? *Brain* **137**, 1676–1700 (2014).

9. Dodd, D. O. et al. Ciliopathy patient variants reveal organelle-specific functions for TUBB4B in axonemal microtubules. *Science* **384**, eadf5489 (2024).

10. Aiken, J., Buscaglia, G., Aiken, A. S., Moore, J. K. & Bates, E. A. Tubulin mutations in brain development disorders: why haploinsufficiency does not explain TUBA1A tubulinopathies. *Cytoskeleton* **77**, 40–54 (2020).

11. Tischfield, M. A. et al. Human TUBB3 mutations perturb microtubule dynamics, kinesin interactions, and axon guidance. *Cell* **140**, 74–87 (2010).

12. Hurd, D. D., Miller, R. M., Núñez, L. & Portman, D. S. Specific α- and β-tubulin isotypes optimize the functions of sensory cilia in *Caenorhabditis elegans*. *Genetics* **185**, 883–896 (2010).

13. Silva, M. et al. Cell-specific α-tubulin isotype regulates ciliary microtubule ultrastructure, intraflagellar transport, and extracellular vesicle biology. *Curr. Biol.* **27**, 968–980 (2017).

14. Simons, C. et al. A de novo mutation in the β-tubulin gene TUBB4A results in the leukoencephalopathy hypomyelination with atrophy of the basal ganglia and cerebellum. *Am. J. Hum. Genet.* **92**, 767–773 (2013).

15. Hersheson, J. et al. Mutations in the autoregulatory domain of β-tubulin 4a cause hereditary dystonia. *Ann. Neurol.* **73**, 546–553 (2013).

16. Leandro-García, L. J. et al. Tumoral and tissue-specific expression of the major human beta-tubulin isotypes. *Cytoskeleton* **67**, 214–223 (2010).

17. Fertuzinhos, S., Legué, E., Li, D. & Liem, K. F. A dominant tubulin mutation causes cerebellar neurodegeneration in a genetic model of tubulinopathy. *Sci. Adv.* **8**, eabf7262 (2022).

18. McFadden, J. R. et al. Clinical, genetic, and structural characterization of a novel TUBB4B tubulinopathy. *Mol. Genet. Metab. Rep.* **36**, 100990 (2023).

19. Maasz, A. et al. TUBB4B gene mutation in Leber phenotype of congenital amaurosis syndrome associated with early-onset deafness. *Eur. J. Med. Genet.* **65**, 104471 (2022).

20. Medina, G., Perry, J., Oza, A. & Kenna, M. Hiding in plain sight: genetic deaf-blindness is not always Usher syndrome. *Cold Spring Harb. Mol. Case Stud.* https://doi.org/10.1101/mcs.a006088 (2021).

21. Renthal, R., Schneider, B. G., Miller, M. M. & Ludueña, R. F. Betal. V. is the major beta-tubulin isotype in bovine cilia. *Cell Motil. Cytoskeleton* **25**, 19–29 (1993).

22. Perry, B., Jensen-Smith, H. C., Ludueña, R. F. & Hallworth, R. Selective expression of beta tubulin isotypes in gerbil vestibular sensory epithelia and neurons. *J. Assoc. Res. Otolaryngol.* **4**, 329–338 (2003).

23. Jensen-Smith, H. C., Ludueña, R. F. & Hallworth, R. Requirement for the betal and betaIV tubulin isotypes in mammalian cilia. *Cell Motil. Cytoskeleton* **55**, 213–220 (2003).

24. Sewell, M. T., Legué, E. & Liem, K. F. Tubb4b is required for multi-ciliogenesis in the mouse. *Development* https://doi.org/10.1242/dev.201819 (2023).

25. Lu, X. & Sipe, C. W. Developmental regulation of planar cell polarity and hair-bundle morphogenesis in auditory hair cells: lessons from human and mouse genetics. *Wiley Interdiscip. Rev. Dev. Biol.* **5**, 85–101 (2016).

26. Zetes, D. E., Tolomeo, J. A. & Holley, M. C. Structure and mechanics of supporting cells in the guinea pig organ of Corti. *PLoS ONE* **7**, e49338 (2012).

27. Szarama, K. B., Gavara, N., Petralia, R. S., Kelley, M. W. & Chadwick, R. S. Cytoskeletal changes in actin and microtubules underlie the developing surface mechanical properties of sensory and supporting cells in the mouse cochlea. *Development* **139**, 2187–2197 (2012).

28. Chen, T. et al. Cochlear supporting cells require GAS2 for cytoskeletal architecture and hearing. *Dev. Cell* **56**, 1526–1540.e1527 (2021).

29. Renauld, J., Johnen, N., Thelen, N., Cloes, M. & Thiry, M. Spatio-temporal dynamics of β-tubulin isotypes during the development of the sensory auditory organ in rat. *Histochem Cell Biol.* **144**, 403–416 (2015).

30. Ludueña, R. F. A hypothesis on the origin and evolution of tubulin. *Int Rev. Cell Mol. Biol.* **302**, 41–185 (2013).

31. Vent, J. et al. Direct involvement of the isotype-specific C-terminus of beta tubulin in ciliary beating. *J. Cell Sci.* **118**, 4333–4341 (2005).

32. Furness, D. N., Hackney, C. M. & Steyger, P. S. Organization of microtubules in cochlear hair cells. *J. Electron Microsc Tech.* **15**, 261–279 (1990).

33. Abdala, C. & Visser-Dumont, L. Distortion product otoacoustic emissions: a tool for hearing assessment and scientific study. *Volta. Rev.* **103**, 281–302 (2001).

34. Michanski, S. et al. Mapping developmental maturation of inner hair cell ribbon synapses in the apical mouse cochlea. *Proc. Natl. Acad. Sci. USA* **116**, 6415–6424 (2019).

35. Gale, J. E., Marcotti, W., Kennedy, H. J., Kros, C. J. & Richardson, G. P. FM1-43 dye behaves as a permeant blocker of the hair-cell mechanotransducer channel. *J. Neurosci.* **21**, 7013–7025 (2001).

36. Pinto, L. H., Invergo, B., Shimomura, K., Takahashi, J. S. & Troy, J. B. Interpretation of the mouse electroretinogram. *Doc. Ophthalmol.* **115**, 127–136 (2007).

37. Kinoshita, J. & Peachey, N. S. Noninvasive electroretinographic procedures for the study of the mouse retina. *Curr. Protoc. Mouse Biol.* **8**, 1–16 (2018).

38. Chacon-Camacho, O. F. & Zenteno, J. C. Review and update on the molecular basis of Leber congenital amaurosis. *World J. Clin. Cases* **3**, 112–124, (2015).

39. Koenekoop, R. K. An overview of leber congenital amaurosis: a model to understand human retinal development. *Surv. Ophthalmol.* **49**, 379–398 (2004).

40. Hoang, T. et al. Gene regulatory networks controlling vertebrate retinal regeneration. *Science* **370**, eabb8598 (2020).

41. Randazzo, D. et al. Persistent upregulation of the β-tubulin tubb6, linked to muscle regeneration, is a source of microtubule disorganization in dystrophic muscle. *Hum. Mol. Genet.* **28**, 1117–1135 (2019).

42. Lu, Y. et al. Single-cell analysis of human retina identifies evolutionarily conserved and species-specific mechanisms controlling development. *Dev. Cell* **53**, 473–491.e479 (2020).

43. Tolomeo, J. A. & Holley, M. C. Mechanics of microtubule bundles in pillar cells from the inner ear. *Biophys. J.* **73**, 2241–2247 (1997).

44. Kolla, L. et al. Characterization of the development of the mouse cochlear epithelium at the single cell level. *Nat. Commun.* **11**, 2389 (2020).

45. Saito, K. & Hama, K. Structural diversity of microtubules in the supporting cells of the sensory epithelium of guinea pig organ of Corti. *J. Electron. Microsc.* **31**, 278–281 (1982).

46. Tucker, J. B., Paton, C. C., Richardson, G. P., Mogensen, M. M. & Russell, I. J. A cell surface-associated centrosomal layer of microtubule-organizing material in the inner pillar cell of the mouse cochlea. *J. Cell Sci.* **102**, 215–226 (1992).

47. Renauld, J., Thelen, N., Bartholomé, O., Malgrange, B. & Thiry, M. Dispensability of tubulin acetylation for 15-protofilament microtubule formation in the mammalian cochlea. *Cell Struct. Funct.* **46**, 11–20 (2021).

48. Fukushige, T. et al. MEC-12, an α-tubulin required for touch sensitivity in *C. elegans*. *J. Cell Sci.* **112**, 395–403 (1999).

49. Savage, C. et al. mec-7 is a beta-tubulin gene required for the production of 15-protofilament microtubules in *Caenorhabditis elegans*. *Genes Dev.* **3**, 870–881 (1989).

50. Cueva, JuanG., Hsin, J., Huang, KerwynC. & Goodman, MiriamB. Posttranslational acetylation of α-tubulin constrains protofilament number in native microtubules. *Curr. Biol.* **22**, 1066–1074 (2012).

51. Ti, S. C., Alushin, G. M. & Kapoor, T. M. Human β-tubulin isotypes can regulate microtubule protofilament number and stability. *Dev. Cell* **47**, 175–190.e175 (2018).

52. Luo, W. et al. Cilia distribution and polarity in the epithelial lining of the mouse middle ear cavity. *Sci. Rep.* **7**, 45870 (2017).

53. Ibañez-Tallon, I., Gorokhova, S. & Heintz, N. Loss of function of axonemal dynein Mdnah5 causes primary ciliary dyskinesia and hydrocephalus. *Hum. Mol. Genet.* **11**, 715–721 (2002).

54. Li, X. et al. Otitis media in sperm-associated antigen 6 (Spag6)-deficient mice. *PLoS ONE* **9**, e112879 (2014).

55. Qin, Z., Wood, M. & Rosowski, J. J. Measurement of conductive hearing loss in mice. *Hearing Res.* **263**, 93–103 (2010).

56. Bittermann, E. et al. Differential requirements of tubulin genes in mammalian forebrain development. *PLoS Genet.* **15**, e1008243–e1008243 (2019).

57. Latremoliere, A. et al. Neuronal-specific TUBB3 is not required for normal neuronal function but is essential for timely axon regeneration. *Cell Rep.* **24**, 1865–1879.e1869 (2018).

58. Williams, D. S. Usher syndrome: animal models, retinal function of Usher proteins, and prospects for gene therapy. *Vis. Res.* **48**, 433–441 (2008).

59. Calabro, K. R. et al. A novel mouse model of MYO7A USH1B reveals auditory and visual system haploinsufficiencies. *Front. Neurosci.* https://doi.org/10.3389/fnins.2019.01255 (2019).

60. Sahly, I. et al. Localization of Usher 1 proteins to the photoreceptor calyceal processes, which are absent from mice. *J. Cell Biol.* **199**, 381–399 (2012).

61. Mattapallil, M. J. et al. The Rd8 mutation of the Crb1 gene is present in vendor lines of C57BL/6N mice and embryonic stem cells, and confounds ocular induced mutant phenotypes. *Investig. Ophthalmol. Vis. Sci.* **53**, 2921–2927, (2012).

62. Montgomery, S. C. & Cox, B. C. Whole mount dissection and immunofluorescence of the adult mouse cochlea. *J. Vis. Exp.* https://doi.org/10.3791/53561 (2016).

63. Livak, K. J. & Schmittgen, T. D. Analysis of relative gene expression data using real-time quantitative PCR and the 2(-delta delta C(T)) method. *Methods* **25**, 402–408 (2001).

64. Vandesompele, J. et al. Accurate normalization of real-time quantitative RT-PCR data by geometric averaging of multiple internal control genes. *Genome Biol.* https://doi.org/10.1186/gb-2002-3-7-research0034 (2002).

Author contributions
U.S. experimental conception, experimental design, data acquisition, data analysis, data interpretation, manuscript writing, and manuscript revision. H.B.P. data acquisition and data analysis. P.T.R.B. data acquisition and data analysis. T.S. data acquisition. S.B.R. data acquisition. T.G. data acquisition. N.B. data analysis, and manuscript revision. S.E.B. manuscript revision, provided tissue samples. C.L.C. experimental design, data interpretation, and manuscript revision. C.T.A. experimental design, data interpretation, and manuscript revision. V.R. experimental conception, experimental design, data interpretation, and manuscript revision.

Competing interests
The authors declare no competing interests.

Additional information
Supplementary information The online version contains supplementary material available at https://doi.org/10.1038/s42003-024-06867-2.

Correspondence and requests for materials should be addressed to Visvanathan Ramamurthy.

Peer review information *Communications Biology* thanks Kristen Rak, Hao Wu and the other, anonymous, reviewer for their contribution to the peer review of this work. Primary Handling Editors: Christian Wozny and Dario Ummarino. A peer review file is available.

Reprints and permissions information is available at http://www.nature.com/reprints

Publisher's note Springer Nature remains neutral with regard to jurisdictional claims in published maps and institutional affiliations.